CHANNELING MEASUREMENTS OF DAMAGE IN ION BOMBARDED IRON

CHANNELING MEASUREMENTS OF DAMAGE IN ION BOMBARDED IRON

by

S. SCHAFER

PART A: McMASTER (ON-CAMPUS) PROJECT*

A Project Report* Submitted in Partial Fulfillment
of the Requirements for the Degree of
Master of Engineering

Department of Engineering Physics
McMaster University
Hamilton, Ontario

April, 1977

*One of two project reports. The other one is designated PART B: OFF-CAMPUS PROJECT.

MASTER OF ENGINEERING (1977)
Department of Engineering Physics

McMASTER UNIVERSITY
Hamilton, Ontario

TITLE: Channeling Measurements of Damage in Ion Bombarded Iron

AUTHOR: Steve Schafer, B.Sc. (McGill University)

SUPERVISOR: Dr. D.A. Thompson

NUMBER OF PAGES: xi, 79

CONTENTS

ABSTRACT

This project is concerned with medium energy heavy ion (60 KEV ^{75}As, ^{40}Ar, 120 KEV $^{150}As_2$) implantation into single crystal iron at room temperature and 35°K. Resulting crystal properties are measured using the technique of high energy light ion (1.0 MEV ^{4}He) channeling and backscattering. The phenomenon of oxygen recoil implantation by the bombarding ion is found to be an important effect to avoid if radiation damage is to be measured. In cases where oxygen recoil implantation has been eliminated, radiation damage was evident from an increase in the minimum channeling yield. The existence of damage beyond the expected damage range at room temperature is attributed to diffusion of defects. Some annealing of damage is observed in samples which have been damaged at 35°K and warmed to room temperature. At doses of about 10^{16} atoms/cm^2, 80(±10)% of the implanted As is found to be at lattice sites.

The merits and limitations of this technique as a simulation of 14 MEV neutron radiation damage are also discussed.

ACKNOWLEDGEMENT

The author wishes to express his gratitude to Dr. D.A. Thompson for suggesting this work, and for his constant advice, attention, and tutorage. Many thanks are due to Bob Walker for his patient instruction on the use of the experimental apparatus and some illuminating discussion. Dr. A. Golanski has contributed to ideas which are incorporated in this work, for which the author is greatly appreciative.

LIST OF TABLES

LIST OF FIGURES

1. INTRODUCTION

Of particular interest to the technology of fast breeders and fusion reactor systems is the intense high energy neutron irradiation to which structural materials will be subjected. Notably, the first wall of a D-T reactor, the most promising fusion energy source, would be subjected to 14 MEV neutron fluxes as high as 4×10^{14} neutrons/cm^2/sec, as well as energy fluxes of up to 900 watts/cm^2.[1] It is presently thought that the body-centered-cubic (B.C.C.) refractory metals may be suitable to withstand the resultant extreme temperatures and irradiation induced damage.[2]

One difficulty common to radiation damage studies in both breeder and fusion reactors, is the absence of high neutron flux test facilities to effectively simulate lifetime ($\sim$20-30 years) radiation fluences in reasonable time periods. One particular difficulty associated with studying radiation damage by 14 MEV neutrons is the non-existence of any neutron source of the necessary energy and intensity. These difficulties suggest that the development of techniques to simulate high energy neutron damage is an essential aspect of current fusion research.

It has been suggested[3] very early on in the study of reactor materials, that the investigation of radiation damage induced by heavy ion bombardment could be used to effectively simulate high energy neutron damage. Chapter 2 of this paper will discuss the benefits and limitations of this technique.

Most early work on radiation damage induced by ion bombardment consisted of studying thin ($\sim$500-1000 Å) single crystal metal films under the transmission electron microscope (TEM), searching for black dots and loop-like features which appear on the samples after bombardment.[3] It has been confirmed[4] that these are point defect aggregates resulting from the impact of heavy ions.

More recently, radiation damage induced by heavy ion bombardment has been studied using the channeling and backscattering of MEV light ions. The channeling effect (see Chapter 3) has met with considerable success in the study of ion-implanted semi-conductors,[5,6] and is currently being applied[7,8] to the study of crystal parameters and radiation damage in ion implanted metals.

In Chapters 4 and 5 we describe an experiment where 60 KEV ions of ^{75}As and ^{40}Ar and 120 KEV $^{150}As_2$ are used to bombard carefully prepared single crystal iron at various doses ($\sim 10^{15}$-10^{16} atoms/cm^2) and temperatures (room temperature – 35 K), and the effects on the crystal lattice are measured using the channeling and Rutherford backscattering of 1.0 MEV He^+ ions. While the primary purpose of the study was to measure heavy ion induced radiation damage in iron and relate this to high energy neutron irradiation, we also discuss the effects of impurities introduced into the sample during the irradiation, impurities such as recoil implanted oxygen and the bombarding particle itself. These latter effects are important not only from a physics point of view, but because they may introduce changes in the lattice which are not attributable to radiation damage. These changes must be fully understood if the technique is to be successful for the study of radiation damage.

2. COMPARISON WITH NEUTRON DAMAGE

Irradiating metals with neutrons and other atomic particles produces defects by direct collision processes. The elementary defects, such as vacancies, interstitials, and dislocations, and more complicated defects such as the nucleation of stable voids resulting in swelling,[9] can have serious effects on the mechanical properties of the irradiated materials. Another direct effect of irradiation is sputtering.[2] This could have major implications in the surface erosion of first wall materials in a fusion reactor. Also in the case of fusion reactors, an indirect effect of radiation damage would be blistering[10] inside the material due to the formation of bubbles of helium gas which are produced through transmutation reactions or possibly injected directly from the plasma.

Ideal simulations of fast neutron radiation damage would precisely reproduce the same effects, such as rate of atom displacement, transmutation product rates, spatial distribution of damage, and the primary knock-on atom (PKA) energy spectrum. In addition, the simulation would not cause effects which are not produced by neutron irradiation, such as alteration of material metallurgy or defect kinetics.

The technique of using heavy ion bombardment in the KEV range can yield useful information on neutron irradiation damage with easily available equipment such as ion implanters and accelerators. 14 MEV neutrons irradiating iron will transmit a mean recoil energy of 199 KEV[11] to the

PKA from elastic and inelastic processes. Displacement cascades thus initiated constitute a major proportion of neutron induced radiation damage. Hence, self-ion bombardment in the KEV range coupled with the analyzing power of the channeling technique (see Chapters 3 and 4) can be used to study the displacement cascades created by the PKA, as well as simulate a large neutron dose in a short time. This technique can also be used to investigate the annealing characteristics of the lattice produced by the irradiation. We note here that this technique will not produce transmutation products. This latter effect may be studied with high energy light ions, such as MEV protons. If ions other than self-ions are used, impurity effects must be accounted for. High flux ion bombardment may also affect defect kinetics due to the increase in rate of energy deposition.

3. DESCRIPTION OF THE CHANNELING EFFECT AND ITS APPLICATIONS

3-1. The Channeling Effect

Energetic ions travelling in an amorphous material lose energy through a series of elastic collisions with the atomic nuclei of the material and by electronic excitation. Since the atoms are randomly arranged in space, the collisions will be described by random impact parameters. However, in a crystalline target, the atoms are arranged symmetrically in space as a lattice, so that for certain trajectories an ion may encounter a number of lattice atoms at similar impact parameters, and the individual collisions may be said to be correlated. For high energy fast moving particles such as MEV protons or alphas, and for impact parameters where the interaction is due to a screened coulomb potential, the individual deflections at each collision between the ion and the target atom will be small. Consequently, if such a particle is incident along a major crystallographic direction, it will suffer a series of small angle, correlated deflections as it passes by neighbouring atoms in the same row and the ion will be steered or "channeled". The reason for using this latter word can be seen by viewing a crystal along a major crystallographic direction. The lattice arrangement forms channels in the crystal which are bounded by closely packed rows of atoms. An ion incident along this direction will be steered by a succession of small angle deflections with the atoms in the channel walls and will follow some sort of

oscillatory trajectory down the channel. This effect was first suggested by Robinson and Oen,[12] who arrived at their conclusions by computer simulation studies.[13] Subsequently, channeling was verified experimentally by a number of groups.[14,15]

It is useful to look in more detail at the trajectory of a channeled particle, with particular reference to energetic light ions in a lattice of heavy atoms, e.g. MEV alphas in iron. Figure 1a shows the trajectory of an ion having small angle collisions with atoms in a row. At each collision the ion is deflected through a small angle $\Delta\psi$. We will regard that motion as restricted to the plane of the paper, a two-dimensional simplification of the three-dimensional trajectories in a real lattice. The change in momentum suffered in each collision is considered to be extremely small compared to the total ion momentum and the deflection is considered to be almost instantaneous as the ion passes the atom in the row. The trajectory can be regarded as being made up of a series of straight lines, with sudden small changes of direction each time the ion passes close to an atom in the row and experiences the short range interatomic forces. The ion receives a succession of impulses as it passes by the atoms in a row.

An alternative approach is to think of the potential experienced by the ion as an average. The individual atoms in the row together with their individual contributions to the trajectory can then be thought of as a string, with the individual charges due to the atoms in the row replaced by the average charge per unit length along the string. Under these conditions, the force experienced by the ion is not discontinuous but will be an average which may be calculated from the average, or

continuum potential. The trajectory will also be continuously changing, as illustrated in Figure 1b.

The first comprehensive treatment of channeling theory, the continuum model, was given by Lindhard.[16] A great advantage of the continuum model is that it enables one to describe the average properties of an entire beam of ions incident in a crystallographic direction. The theory also defines the criteria for stable and unstable channeling trajectories.

The Lindhard standard potential describing the elastic interaction between an ion and an atom is[16]

$$V(r) = \frac{Z_1 Z_2 e^2}{r}\left\{1 - \frac{r}{(r^2+C^2a^2)^{\frac{1}{2}}}\right\} \qquad 3\text{-}1$$

where C is an adjustable parameter normally set equal to $\sqrt{3}$, r is the distance separating the ion and target atom, Z_1 is the atomic number of the ion, Z_2 is the atomic number of the target atom, e is the electronic charge, and a is the Thomas-Fermi screening radius,

$$a = .4683(Z_1^{2/3} + Z_2^{2/3})^{-\frac{1}{2}}\ \text{Å} \qquad 3\text{-}2$$

The major assumption of the continuum model is in defining an average interatomic potential experienced by an ion at a distance ρ from the atomic string. This potential is given by,

$$U(\rho) = \frac{1}{d}\int_{-\infty}^{\infty} V(\sqrt{Z^2+\rho^2})\,dZ \qquad 3\text{-}3$$

where Z is measured in the direction of the row and d is the distance

between consecutive atoms in the same row.

Using equation 3-1 in 3-3 results in the standard continuum potential, $U(\rho)$, given by

$$U(\rho) = \frac{2Z_1Z_2e^2}{d}\,\phi(\rho/a) \qquad 3\text{-}4$$

where $$\phi(\rho/a) = \frac{1}{2}\,\ell n\{(\frac{Ca}{\rho})^2 + 1\} \qquad 3\text{-}5$$

The continuum model of scattering is only valid for ions which remain relatively far from any atomic string and at low transverse angle, ψ (see Figure 1) to it. The approximation breaks down when an ion has sufficient transverse energy to penetrate into the core of the strings where it may be scattered at large angles from individual atoms. A detailed analysis by Lindhard[16] shows that above a certain transverse angle, ψ_c, the ion will be scattered out of the channel. This critical angle was found to be[16]

$$\psi_c \approx \frac{2Z_1Z_2e^2}{Ed}\,\phi(\frac{1.2x_{rms}}{a})^{\frac{1}{2}} \qquad 3\text{-}6$$

where x_{rms}^2 is the mean square amplitude of vibration of the atom in the row.

When an ion is channeled, it will reach a certain minimum distance, ρ_{min}, to the row and then begin to move away from that row, as in Figure 1. Any interactions that require an impact parameter smaller than ρ_{min} will be excluded. Examples of such excluded reactions are large angle Rutherford scattering and nuclear reactions. Some of the ions will enter the crystal less

than the Thomas-Fermi screening radius, a, from a row, and be scattered by the surface atoms into an angle greater than ψ_c. These ions will either be scattered away from the crystal or enter the crystal in a random direction.

Figure 2 shows the yield of a typical large angle Rutherford backscattering experiment as the impinging ion beam is scanned through a major crystallographic direction. The figure is useful in defining some channeling parameters. We note that the random yield, Y_R, is the yield obtained when the ion beam is travelling into the crystal randomly. For perfect alignment ($\psi = 0°$) most of the beam will be channeled and the so-called minimum aligned yield, Y_A, will result. The normalized minimum backscattered yield is χ_{min} given by[16]

$$\chi_{min} = \frac{Y_A}{Y_R} \approx \pi N d \rho_{rms}^2 \qquad 3\text{-}7$$

where N is the atomic density and

$$\rho_{rms}^2 = a^2 + x_{rms}^2 \qquad 3\text{-}8$$

Also shown in Figure 2 is the half-angle, $\psi_{1/2}$, defined as the semi-angular width midway between Y_A and Y_R. It should be noted here that experimentally measured half-angular widths, $\psi_{1/2}$, are found to be in good quantitative agreement with the theoretically derived critical angles, ψ_c, and the equivalence between the two is often assumed.

Table 1 shows typical values of χ_{min} and $\psi_{1/2}$ for the case of 1.0 MEV He^+ ions backscattered off single crystal iron in various crystallographic directions. The calculations were performed using the empirical

equations of Barrett.[17]

A combination of channeling and Rutherford backscattering has proved to be particularly informative when applied to problems such as radiation damage, annealing, and the location of heavy impurities within the crystal lattice. The principles behind the experimental technique were illustrated by Bøgh,[18] and we shall briefly review them here.

A typical experimental arrangement is shown in Figure 3. A well collimated monoenergetic beam of light particles is fired into an evacuated chamber containing the target crystal mounted on a goniometer. After striking the target some of the beam is scattered and particles scattered within a particular solid angle are detected in a solid state detector mounted within the chamber. The goniometer allows the target to be moved with respect to the beam so that the beam can be aligned in terms of crystallographic directions for single crystals.

The energy spectrum obtained in this manner is shown in Figure 3. The random spectrum is obtained when the beam of particles enters the crystal in a random direction. This spectrum consists of a sharp edge at K^2E_o, where K is the kinematic scattering factor given by

$$K = \left[\frac{M_1\cos\theta + (M_2^2 - M_1^2\sin^2\theta)^{\frac{1}{2}}}{M_1 + M_2}\right] \qquad 3\text{-}9$$

and M_1 is the mass of the bombarding particle, E_o is its energy, M_2 is the mass of the target atoms, and θ is the scattering angle in the laboratory system. The energy K^2E_o corresponds to the bombarding particle suffering large angle Rutherford collisions with the surface atoms and being deflected into the detector. If the projectile is 1.0 MEV He^+,

the target iron, and $\theta = 150°$, the $K^2E_o = 765$ KEV. The sharp edge of the spectrum is followed by a smoothly varying yield at lower energies. Projectiles not scattered at the surface lose energy by inelastic processes as they pass through the lattice before colliding elastically with the target atoms. After collision they again lose energy inelastically as they leave the target on their passage to the detector. A smoothly varying spectrum results, as illustrated in Figure 3. The backscattered yield increases at lower energies (greater depths) because the cross-section for elastic collisions increases as E^{-2}, where E is the energy of the analyzing beam. The backscattering yield as a function of energy can be converted into a yield as a function of depth into the crystal by means of the following formula[18]

$$\Delta t = \Delta E\left[S(E_o)K^2 + S(K^2E_o)\,\frac{\cos\theta_1}{\cos\theta_2}\right]^{-1} \qquad 3\text{-}10$$

where ΔE, Δt, θ_1 and θ_2 are defined in Figure 3. S(E) is the stopping power of the projectile in the target material.

Also shown in Figure 3 is an "aligned" spectrum, i.e. a spectrum obtained with the projectile beam aimed down a major crystallographic axis. Immediately apparent is the large reduced yield. The conditions are ideal for channeling, and a considerable proportion (>95% usually) of the beam is prevented from moving near to the atoms in the lattice rows. Since large angle Rutherford scattering requires small impact parameters, this means that the yield at all depths is reduced below that obtained in a random exposure for the same projectile flux. Note that the yield from collisions at the surface of the sample should be the same

under both random and aligned conditions, since no shadowing can occur from the outer layer of atoms and the Rutherford yield which depends on the number of scattering centres per unit area is the same in both cases. This effect is seen in Figure 3 as a small surface peak at K^2E_o, where the spread of the peak is due to detector resolution. Under usual experimental conditions, a thin layer of damage or oxide will exist on the surface. The random arrangement of target atoms in this layer will also increase the yield from the surface of the crystal. The yield does not fall to zero at depths beyond this surface peak because there are several processes which have the effect of randomizing a fraction of the aligned beam. These processes include scattering from the outer layer of row atoms, scattering in the amorphous surface layer, and scattering from target atoms displaced slightly ($\sim$.1-.2 Å) from the crystal row due to thermal vibrations. The value of $\chi_{min}(t) = Y_A(t)/Y_R(t)$ is called the random fraction of the beam at the depth t.

3-2. Application of Channeling to Ion Bombardment Effects in Metals

3-2-1. Determination of impurity substitutional fraction

The scattering of the projectile from an impurity which is heavier than the target atoms results in less energy loss than scattering from the target atoms, since K^2, defined by equation 3-9, increases with increasing target mass. For example, He^+ scattering from xenon located at the surface of an iron lattice appears at higher energy, as illustrated in Figure 4. With the energies usually employed in ion implantation, the

ranges of heavy ions result in depth distributions close to the sample surface so that well resolved peaks similar to that shown in Figure 4 are obtained.

The location of the implanted ions within the lattice can be investigated by the channeling technique. For exposure of the sample to helium beams in a random direction, all of the beam is capable of interaction with the implanted impurity. No shadowing occurs, and the area under the impurity peak is a direct measure of the number of implanted ions. However, for an aligned exposure, if any of the impurity is shadowed by the crystal row (such as a substitutional lattice site), a reduction in yield will result. The impurity peak area in this case is a measure of those atoms which occupy positions within the open channel and can interact with the beam, plus interaction with the random part of the beam. In order to determine the true substitutional fraction, it is necessary to determine the impurity backscatter yield from at least two major crystallographic directions, such as the <110> and <111>. In this way, the hypothesis that the impurity lies on sites along the row but not on lattice sites can be eliminated if equivalent attenuation of yields is obtained for each direction.

Feldman and Murnick[19] have studied the implantation of 100-200 KEV $^{131,132}Xe$ at doses of 10^{14}-10^{16} ions/cm^2 in single crystal iron at room temperature. They obtained angular distributions and critical angles in good agreement with the Lindhard theory.[16] A summary of their experimental results is shown in Table 2. The important features are that (50±10)% of the Xe is found at lattice sites for low doses ($\sim 1\text{-}2\times10^{14}$ atoms/cm^2), but at higher doses ($\sim 10^{16}$ atoms/cm^2) about 80% of the Xe is

on non-substitutional sites. They also found that there is a substantial reduction in substitutional fraction if the implanted sample is annealed to 450°C, but this effect is not observed if the anneal is performed at 300°C.

3-2-2. Radiation damage

As mentioned in Chapter 1, most early work on radiation damage in metals was studied by electron microscopy. Results obtained in this way can be used not only to test results obtained from other techniques, but can also complement them, providing information which may facilitate their analysis. For example, knowledge of the Burgers vector associated with a particular kind of radiation induced dislocation loop may allow for the calculation of the loop dechanneling cross-section.[20] It is useful, therefore, to review some current work employing transmission electron microscopy to study radiation damage in iron by ion bombardment.

Masters[21] has studied 150 KEV Fe^+ bombardment of cold rolled iron foils. Dislocation loops were observed to increase in diameter from 50 Å to 1500 Å as the irradiation temperature was increased from 20°C to 550°C. It was found that large loops (1000-1500 Å in diameter) suitable for diffraction analysis were produced by doses of $\sim 1.7 \times 10^{16}$ Fe ions/cm^2 with the specimen at a temperature of 550°C. Of particular interest is the fact that the loops were found to be interstitial in nature, and no vacancy loops were observed. The proposed explanation of this effect was that the bombarding Fe^+ ions provide the interstitial atoms directly, and that collision cascades are irrelevant to the formation of these loops. The experimental evidence for this conclusion was that there were

less iron atoms clustered in the loops than entered the foil during the irradiation. The results indicated that only about 1% of the injected interstitials condensed as visible loops.

English et al.[22] have studied the irradiation of polycrystalline foils of α-iron at room temperature with heavy ions (Fe^+, Ni^+, Ge^+, Kr^+, Xe^+ and W^+) at energies between 40 and 200 KEV to doses of $\sim 5 \times 10^{12}$ ions/cm^2 using TEM. The results obtained are shown in Figure 5, which demonstrates the efficiency with which different 80 KEV ions produce visible clusters. The defect yield in Figure 5 is defined as the fraction of cascades which collapse to produce visible clusters. From Figure 5, two important results can be obtained. Firstly, there is no observable damage in self-ion irradiated specimens. This result is consistent with observations of neutron irradiated α-Fe, which showed that no visible damage is produced at doses $\lesssim 5 \times 10^{18}$/cm^2.[23] It was suggested[22] that cascades initiated by self-ions do not collapse, a conclusion which contradicts the stated results of Masters.[21] The second important result was the increasing defect yield as a function of ion mass. This effect was attributed to the fact that increasing the ion mass increased the compactness of the cascade, and increased the density of energy deposited. This can be seen more clearly with reference to Table 3. In this table, $\langle X_D \rangle$ is a measure of the mean damage range, $\langle \Delta X_D^2 \rangle^{\frac{1}{2}}$ is the damage straggling, and $\langle Y_D^2 \rangle^{\frac{1}{2}}$ is the transverse damage straggling. These quantities were calculated by English et al.[22] using the WSS theory.[24] θ_0 is an estimate of the maximum energy density in the cascade, calculated from the theory of Sigmund.[25] Also shown in Table 3 are the same calculations redone for this work, using the updated

theory incorporated in the Winterbon Tables.[26] The number of vacancies per cascade, N_d, was calculated in this work using[27]

$$N_d = \frac{.42\nu(E)}{E_d} \qquad 3\text{-}11$$

where $\nu(E)$ is the energy into atomic collisions and E_d is the displacement energy, taken as 24 eV for Fe.[28] The estimate of the maximum energy density in the cascade has been calculated by[25]

$$\theta_o = \frac{\nu(E)}{(2\pi)^{3/2}\langle \Delta X_D^2 \rangle^{\frac{1}{2}} \langle Y_D^2 \rangle N} \qquad 3\text{-}12$$

where N is the atomic density of the substrate.

It is of interest to note that for the ion-target pairs of English et al.[22] the total number of displacements per cascade is roughly constant. What does alter is the spatial distribution of damage and its depth below the surface, as can be seen from the range and straggling parameters. This affects the maximum energy density in the cascade, θ_o. Figure 6 plots the defect yield of Figure 5 vs. θ_o. It can be seen that as the energy density in the cascade increases, the efficiency with which visible clusters are produced increases significantly. These observations clearly show that if TEM results are to be compared with results from other techniques, such as channeling and Rutherford backscattering, judicious choice of the bombarding ion and its energy are imperative, at least for radiation damage studies in iron. Figure 6 also shows (arrows) the expected defect yield of ions used in this work.

As mentioned in Chapter 1, recent work on radiation damage to semi-conductor single crystal lattices has used the channeling and

Rutherford backscattering technique with great success. The backscattered spectra from these types of experiments show dramatic increases in surface peaks over the depth of the damaging ion penetration. The peaks correspond mostly to the analyzing beam directly scattering off interstitials located in the channel and can be used to calculate the number of displaced atoms/cm^2 and the depth distribution of the damage.[29] These well defined surface peaks have not appeared when applying this same technique to metals, making the analysis considerably more complicated, and in fact, not yet well understood. These points can be amplified with reference to some examples.

Figure 7 shows typical backscattered spectra from a semi-conductor. The large growth in the width and size of the surface peak in the aligned spectra after implantation of 300 KEV Ar^+ ions at 25°K is attributed to scattering from atoms displaced during the bombardment. Displaced atoms increase the measured yield over that for a perfect crystal by two mechanisms:[18]

1. They deflect particles from the aligned beam into the random beam. This is called dechanneling. Once in the random beam, these particles can interact with all atoms.
2. The aligned beam can be backscattered directly from displaced atoms.

Bøgh[18] has shown that the density of displaced atoms, $N_d(t)$, at depth t, is given by

$$N_d(t) = N \cdot \frac{\frac{Y_A(t)}{Y_R(t)} - \chi'(t)}{1 - \chi'(t)} \qquad 3\text{-}13$$

where N is the density of substrate atoms, $Y_A(t)$ is the random yield, and $\chi'(t)$ is the random fraction of the analyzing beam in the damaged crystal.

In order to use equation 3-13, it is necessary to know how the random fraction of the beam, $\chi'(t)$, varies with depth throughout the damaged region. Figure 8 shows the expected shape for this dechanneling; a sharp rise in $\chi'(t)$ throughout the damaged layer until the predicted variation runs smoothly into the measured dechanneling level beyond the damage peak. Also shown in Figure 8 is a linear approximation to the dechanneling curve, which is adequate for many cases.[29] The dechanneling may be due to single events (single scatter dechanneling), several events (plural scattering), or many events (multiple scattering). Methods of calculating the dechanneled fraction shall be discussed later with respect to metals.

The calculation of the number of displaced atoms using the above techniques is not without difficulties and ambiguities. There is not only difficulty in estimating the dechanneled fraction of the analyzing beam, but in many implantation experiments the host lattice will contain displaced atoms and may also be in a state of strain, i.e. with the rows and planes distorted. The measured backscattered yield will contain contributions from these strained regions in the form of increased dechanneling, rather than direct backscatter from interstitials. We shall see that this problem is particularly acute

in metals. Nevertheless, for semi-conductors, the technique has provided valuable information on the depth distribution of radiation damage.

Pronko et al.[30] have studied ion bombardment damage in niobium and tungsten at low (25°K) temperature using the channeling and Rutherford backscattering technique. The damage was created by 300 KEV Ar^+ at doses of 10^{13}-10^{15} atoms/cm^2. The spectra obtained from unimplanted and implanted tungsten are displayed in Figure 9a. The shape of the implanted spectra is typical of metals. The surface peak is shown to increase negligibly after dechanneling is taken into account, and the minimum yield behind the peak increases compared to the unimplanted sample. The rate of dechanneling in the damaged region with respect to distance into the crystal is significantly larger than in the undamaged region. The importance of this will be examined shortly. Figure 9b shows the spectra obtained from niobium. Note that in this case there is a slight indication of a damage peak at $\sim$1000 Å, which is consistent with the mean damage depth of 300 KEV Ar in niobium theoretically calculated[26] (see Table 3). Both samples (tungsten and niobium) were annealed to 300°K for 12-16 hours, then recooled, and the aligned backscattering spectra were remeasured. In the case of tungsten, no change in the backscattered spectrum was observed, indicating an absence of significant annealing between 25°K and 300°K. It was pointed out that this conclusion conflicted with previous resistivity[31] and field-ion-microscopy[32] measurements, which clearly showed the existence of prominent anneal stages between 25°K and 100°K. No resolution of this difficulty was proposed. In the case of niobium, annealing the sample caused the disappearance of the damage peak, as shown in Figure 9b. However, the damage did not completely anneal out, as proven by a comparison

of χ_{min} after the anneal with that of the unimplanted sample. The conclusions of this work were that some damage in niobium was due to interstitials, but that most of the damage in both niobium and tungsten was due to defects which primarily affect the dechanneling rate, such as lattice strains and dislocation loops.

Gettings et al.[7] have applied the channeling and Rutherford backscattering technique to the study of radiation damage in ion implanted vanadium. They used Ga, Bi, In, Cs, Se and Kr ions in the energy range between 40 and 300 KEV and doses in the range 10^{14}-10^{17} atoms/cm^2. In order to at least qualitatively estimate the damage, some useful parameters were defined. These are shown in Figure 10, where Y_D/Y_R was taken as a simple damage parameter, to give a relative picture of the radiation damage with changing impurity dose or energy. X_D is the distance between the surface channel (taken at the half height of the random edge) and the "knee" in the channeled spectra, and was described as the mean depth of radiation damage. This parameter is better characterized as the distance into the sample where the radiation damage becomes negligible, since it is clear that at X_D the dechanneling begins to assume a slope close to the undamaged crystal.

Figures 11 and 12 show some results from this work. Two features of Figure 11 are worth noting. Firstly, even at doses of 10^{17} Ga atoms/cm^2, the damage has still not saturated. Similar behavior was observed for the other impurities. A second important feature is that the damage (as defined by the Y_D/Y_R parameter) is approximately the same for the 150 KEV Ga^+ and the 300 KEV Bi^+. In general, it was found that impurities implanted over approximately the same projected range, $\langle x_D \rangle$, for the same doses, exhibited

only a slight variation in damage. This effect contradicted the expected results from a straight forward consideration of the amount of energy going into nuclear stopping. Table 3, shows, for example, that Bi incident at 300 KEV would give up almost three times as much energy to nuclear stopping as 150 KEV Ga. In order to explain this anomaly, it was suggested that recombination of vacancy-interstitials occurred during implantation resulting in similar damage levels.

Figure 12 shows the difference between the depth of damage and the projected range vs. dose. It was suggested that the existence of damage far beyond the mean depth of ion projected range calculated by Lindhard theory could be explained by some mechanism whereby defects diffuse during implantation.

If the aligned, damaged backscattered spectra are to be used effectively for extracting information about the damage, a comprehensive understanding of dechanneling phenomena is required. Quéré[20] has pointed out that the conditions under which a given number of implantation created defects react and cluster have a major influence on the dechanneling cross-section. Furthermore, it was argued that for defects which distort the lattice, such as dislocations, dechanneling may occur before as well as beyond the defect. These points emphasize some inherent difficulties which must be accounted for in any systematic treatment of dechanneling in metals.

Davies et al.[33] have investigated the dechanneling of MEV protons in tungsten. It was found that in the (110) planar case, the dechanneling rate was almost independent of temperature and inversely proportional to the proton energy, as predicted by theory. In the <111> axial case, the

dechanneling rate was found to be almost independent of energy, in contrast with theory which predicts a 1/E dependence. The dechanneling rate depended strongly on temperature, but not as strongly as ρ_{rms}^2 (defined in 3-1) as predicted by theory. These anomalies have not been explained, and they illustrate clearly that even dechanneling in undamaged crystals is not well understood. The dechanneling in the damaged crystal may depend in some complicated fashion on energy[20] or temperature and on the amount, type, and distribution of defects, and so represents an even more formidable problem.

There have been some attempts at extracting damage depth profiles from the backscattered spectra of ion bombarded metals. The general procedure is to assume single scatter dechanneling[18] or multiple-scatter dechanneling,[34] and then use the basic equations for dechanneling to extract the profiles. For single-scatter dechanneling[8]

$$N_d(t) = -\frac{1}{\sigma_{ss}} \frac{d}{dt} \left[\ell n\left(\frac{1 - \chi'(t)}{1 - \chi(t)}\right)\right] \qquad 3\text{-}14$$

where $N_d(t)$ is the volume concentration of defects, $\chi(t)$ and $\chi'(t)$ are the measured dechanneled fraction before and after damage respectively, and σ_{ss} is the single scatter dechanneling cross-section per displaced atom, calculated by integrating the Rutherford cross-section from the critical angle (ψ_c) to π. Hence

$$\sigma_{ss} = \frac{\pi Z_1 Z_2 e^2 d}{2E} \qquad 3\text{-}15$$

For multiple scattering,[8]

$$N_d(t) = -\frac{1}{\sigma_{ms}} \frac{d}{dt} [\ell n(\frac{\chi'(t) - \chi(t)}{1 - \chi(t)}]^{-1} \qquad 3\text{-}16$$

where σ_{ms} is the multiple scattering dechanneling dechanneling cross-section, given by

$$\sigma_{ms} = \tfrac{1}{2}\pi\psi_c^2 d^2 \ell n(1.29\varepsilon) \qquad 3\text{-}17$$

where ψ_c is the critical angle for scattering out of the channel, and ε is the Lindhard dimensionless energy parameter.

Pronko[8] discussed the contributions of each dechanneling mechanism for .27 and 2.0 MEV He^+ beams channeled in gold. He concluded that single-scatter dechanneling is dominant for the former energy, and multiple scattering will dominate the latter. This is qualitatively reasonable since a slower particle will have greater sensitivity to dechanneling by a single defect. Figure 13 shows the results of room temperature 540 KEV self-ion irradiations of Au at various fluences. These depth profiles show little agreement with the predictions of random stopping theory, from which a mean damage depth of $\sim$280 Å is calculated[26] for 540 KEV Au irradiation of Au. The unexpected broadness and deepness of the profiles were assumed to be caused by unavoidable heavy-ion channeling. This conclusion may be contrasted with that of Gettings et al.,[7] where a defect diffusion mechanism was postulated to account for the deep damage. Also apparent from Figure 13 is a double hump appearing in the depth profile at low fluences. This effect was explained by assuming that the loss of interstitials to the surface of the sample results in a reduction of the vacancy-interstitial recombination in that

region. In the central region, randomly moving interstitials recombine with vacancies before reaching the surface. As the irradiation proceeds and steady state conditions are approached a more uniform distribution is achieved. It is also pointed out that the precise defect profile at any irradiation fluence will be controlled by parameters associated with the kinetic processes of importance before and after the irradiation. These parameters can be specimen temperature, activation energy for interstitial and vacancy migration, sink density, film thickness, etc.

The profiles of Figure 13 were calculated using equation 3-14. The function to be differentiated in 3-14 was calculated point by point from the observed spectra, and then a smooth multiple-order polynomial curve was fit to these points. This polynomial was used as the integral damage profile and was differentiated to yield the final volume distribution. It was pointed out that this method eliminates statistical counting fluctuations and experimental noise. The errors in the depth profiles will be related to the errors in calculating the differentials, which may be particularly severe at low doses, where the differences in $\chi'(t)$ and $\chi(t)$ may be of the same order as the experimental errors. Furthermore, it should be pointed out that the absolute volume concentration of defects shown in Figure 13 may be significantly in error due to the choice of equation 3-15 for the dechanneling cross-section. In metals, where radiation damage takes the form of lattice strain and dislocation loops, it may not be correct to think of dechanneling as resulting from scattering from one defect. In fact, strain fields may act on the particle over many atomic layers, increasing its transverse energy and thus contributing to dechanneling.

Pronko and Merkle[35] have performed similar experiments on Au, and have calculated dimensions of the collision cascades that are qualitatively consistent with theory. The primary assumptions made in order to perform the calculations were:

1. The cluster production rate will be proportional to the undisturbed lattice volume $1-NV_o$, where N is the number of cascades per unit volume and V_o is the volume per cascade. Hence

$$\frac{dN}{d\phi} = \frac{1}{t}(1-NV_o) \qquad 3\text{-}18$$

where ϕ is the fluence, t is the depth over which the damage is distributed, taken to be 1000 Å as a first approximation.

2. For low damage concentrations,

$$N = \phi/t \qquad 3\text{-}19$$

3. $$N\sigma_d = \frac{d\chi}{dt}\left(\frac{1}{1-\chi_{min}}\right) \qquad 3\text{-}20$$

where $\frac{d\chi}{dt}$ is the slope of the dechanneled fraction, χ_{min} is the ratio of the minimum yield of the damaged spectrum to the random yield at the surface, and σ_d is the dechanneling cross section. We recognize this as a slight simplication to single scatter dechanneling.

From 3-19 and 3-20, it can be seen that the low dose slope of a graph with ϕ along the abscissa, and $\frac{d\chi}{dt}\left(\frac{1}{1-\chi_{min}}\right)$ along the ordinate is simply equal to σ_d/t, and hence σ_d is calculated. From 3-18, a graph of $\sigma_d \frac{dN}{d\phi}$ vs. $\sigma_d N$ gives V_o, the volume per cascade, which was then assumed to be roughly spherical. Hence the radius of the cascade is calculated.

In this way, they calculated a cascade radius of 194 Å for 540 KEV Au^+ in Au. By comparison, theoretical calculations[26] show a relative

damage straggling of 172 Å and a relative transverse damage straggling of 115 Å. Similarly, for 270 KEV Au^+ on Au, 138 Å was the experimental result for the cascade radius using the above procedure, and 102 Å and 70 Å are the theoretically calculated[26] relative damage straggling and relative transverse damage straggling respectively.

4. EXPERIMENTAL

Figure 14 is a schematic drawing of the McMaster ion implantation and channeling facility used to perform the experiments. The usual procedure was to obtain aligned (<110> and <111>) and random backscattered spectra from a clean, undamaged single crystal of iron, then to carry out the bombardment, and finally to observe the post-implanted backscattering properties of the iron-impurity system. Separate experiments were performed with the sample at room temperature and cooled to 35°K by a cryorefrigerator. The combined accelerator system allowed the implants and Rutherford backscattering analysis to be performed under identical environmental conditions (i.e. temperature and pressure).

Figure 15 shows schematically the details of the target chamber. Surrounding the sample on the goniometer is an insulated copper tube (cryo-shield) which is thermally and electrically connected to the sample for low temperature experiments, and thermally isolated from the sample for room temperature experiments. This cryo-shield is also thermally connected to and electrically isolated from the cryorefrigerator, and hence acts as a cryopump, improving the vacuum in the target region to $\lesssim 10^{-9}$ torr which reduces the surface contamination during the experiment. No carbon buildup was observed during a 15-20 hour experiment. The shield also acts as a Faraday cup to assure accurate dose measurements. The amount of impurity implanted is also checked by evaluating the scattering intensity in its own backscatter peak, verifying the dosimetry to better

than 10%. Surrounding the cryo-shield is a copper heat radiation shield, which is continuously cooled by a flow of liquid nitrogen. Aluminum inserts in the tubes leading to the solid state (surface barrier) detectors minimize the effects of low angle backscatter from the tube walls. A heater in the sample head allows the sample temperature to be maintained at least 30° above that of the cryo-shield during cooldown, minimizing impurity buildup on the target surface.

The single crystals of iron ((110) surface), kindly supplied by Dr. J.A. Davies, were first degreased in trichloroethylene, rinsed in methanol, followed by etching for 4-5 minutes in a solution consisting of 168 mls de-ionized water, 8.4 gms of oxalic acid, and 12 mls of 30% H_2O_2 at 40-45°C. The samples were stored in methanol for approximately 15 minutes prior to being mounted on a 2-axis goniometer and placed in the target chamber. The samples were exposed to atmosphere for periods of 10-15 minutes during this procedure.

Crystal quality can be inferred from the channeled beam minimum backscattered yield, χ_{min}, obtained along the <110> and <111> axes. Typical experimental and theoretical values are shown in Table 1. The wide disparities between experimental and theoretical values may indicate that the method of sample preparation was not adequate. Feldman and Murnick[19] found similar results by mechanical polishing and then electropolishing (see Table 1). It should also be pointed out that the previous history of the crystal used in these experiments was unknown. Therefore it is difficult to determine the reasons for the large minimum yields obtained. One explanation for the high χ_{min}'s in the <111> direction could be in the fact that the 1.0 MEV He^+ probe is travelling

through a thicker oxide layer, leading to increased dechanneling. This is because the sample is tilted ∿35° from the surface normal for channeling in the <111> direction.

Also shown in Table 1 is an experimental value and theoretical values of half angular widths, $\psi_{\frac{1}{2}}$, at half normal yield. Good agreement is obtained for the <110> low temperature case. Experimental values for the other cases were not obtained.

Figure 16 shows typical energy spectra of backscattered 1.0 MEV He^+ ions incident parallel to the <110> axis for implanted and unimplanted Fe. The area under the iron surface peak for the unimplanted spectrum corresponds to a layer of $\sim 1.0 \times 10^{16}$ Fe atoms/cm^2, or, assuming that it is primarily due to a layer of iron oxide, corresponds to about 26 Å of Fe_2O_3. Bøgh[36], using the double alignment technique for greater sentitivity to the oxygen and iron surface peak, has verified the stoichiometry Fe_2O_3, and measured an oxide thickness of ∿30 Å for his crystal.

It was noted in Chapter 2 that self-ion bombardment is a method of reproducing neutron induced displacement cascades. For these types of experiments, an Fe^+ ion would represent the primary knock-on atom (PKA). However, sufficient beam currents of Fe were not obtained. The irradiations consisted of various doses ($\sim 10^{15}$-10^{16} ions/cm^2) of 60 KEV As^+ and Ar^+ at room temperature and 35 K, and one low temperature irradiation with 120 KEV As_2^+. Typical beam currents were 600-700 nA/cm^2. The beam was reduced to 2 mm diameter by an off-axis aperture and then X-Y swept across a 4 mm aperture in front of the sample to ensure a uniformly bombarded area, and to ensure that any particles which become neutralized before the sweep system could not strike the target.

The channeling measurements were performed in-situ using 1.0 MEV He^+ ions collimated to half angle divergence of 0.037°. Typical analyzing beam currents were .5-3 nA/mm^2, depending on the detector dead time, which was maintained at <5%. Typical doses to obtain a spectrum were 5-10 $\mu C/mm^2$. It was found that doses of 50-60 $\mu C/mm^2$ had no measurable effect on the He^+ backscattered spectrum.

5. RESULTS AND DISCUSSION

5-1. Oxygen Recoil Implantation

Two cryorefrigerators were employed for the low temperature experiments, one which had a base temperature of ∿65°K for the cold shield-target combination, and one which had a base temperature of ∿35°K for the target with the cold shield 5-10°K lower. At the lower temperature, it was found that the chamber pressure was at least one order of magnitude lower than at the higher temperature (∿10^{-7} torr for the lower temperature, ∿10^{-6} torr for the higher temperature), and probably several orders of magnitude lower near the target surface due to improved cryopumping. Figure 17 shows the spectra obtained at both 35°K and 65°K for approximately equivalent doses of 60 KEV As^+. It can be seen that the 65°K implant produces a Rutherford backscattering spectrum which is significantly different from the 35°K implant. The former spectrum contains an enhanced surface peak, increased dechanneling, and an impurity peak starting at backscattered energy ∿387 KEV. It was determined that this impurity peak corresponded to backscatter from O^{16}, since $K^2E_o(O^{16})$ ∿383 KEV. For N^{14}, K^2E_o ∿.333 KEV, and no trace of nitrogen was found in the backscattered spectrum. The 35°K implant spectrum is characteristic of metals, as discussed in Chapter 3.

In order to obtain more information on the source of the oxygen, and its effects on the backscatter spectrum, a bombardment was carried out at 65°K using 64 KEV Ar^+ at about the same dose as the As^+ implants.

The resulting spectrum from this experiment is shown in Figure 18. It can be seen that the oxygen peak area is down by a factor of about 2, and an enhanced surface peak remains, though smaller than the As^+ bombardment. Furthermore, the dechanneling in the damaged region assumes the characteristic shape of metals discussed in Chapter 3.

It is interesting to try and determine where the oxygen comes from, and how its presence is affecting the lattice. We shall now propose a model which accounts satisfactorily for both the amount of oxygen present, and the type of backscattering spectrum observed.

We suggest that a supply of oxygen in the chamber is continually being adsorbed on the surface of the target and that the bombarding ion is recoil implanting the oxygen into the target. If we assume that for every oxygen atom implanted, a new oxygen atom is adsorbed on the target surface, then the change in the number of oxygen atoms/cm^2 on the target surface, $dN_0(\phi)$, is equal to the amount of oxygen which is recoil implanted by the fluence, $d\phi$, i.e.

$$dN_0(\phi) = N_0(\phi)\sigma d\phi \qquad 5\text{-}1$$

where σ is the total cross section for a collision between the bombarding ion and an oxygen atom.

We can solve equation 5-1 to yield,

$$\sigma = \frac{1}{\phi_o} \ln \frac{N_0(\phi_o)}{N_0(0)} \qquad 5\text{-}2$$

where ϕ_o is the total dose of bombarding ions in particles/cm^2. $N_0(0)$ is the number of oxygen atoms in the unimplanted crystal. This number can

be determined from the iron surface peak in the unimplanted crystal and an assumption on the stoichiometry of the oxide surface of the unimplanted crystal. As discussed in Chapter 4, we assume the oxide to be Fe_2O_3, giving $N_0(0) = 1.5 \times 10^{16}$ atoms/cm^2. This number is correct to within 10% if the assumption on the stoichiometry is correct.

The right side of equation 5-2 can be determined from experimental results. In order to determine the left hand side, we note that for a $1/r^2$ elastic scattering potential, the differential cross-section is given by Lindhard et al.[37],

$$d\sigma(T) = \frac{.327\pi a^2 T_m^{\frac{1}{2}} dT}{2\varepsilon T^{3/2}} \qquad 5\text{-}3$$

where a is the Thomas-Fermi screening radius given by equation 3-2, T is the energy transfer of the collision, T_m is the maximum energy transfer possible, and ε is the projectile energy in dimensionless units[37]. Integrating equation 5-3 from T_1, (some arbitrary minimum energy transfer possible in a collision), to T_m, we obtain the total collision cross-section, σ,

$$\sigma = \frac{.327\pi a^2}{\varepsilon} \left\{ \left(\frac{T_m}{T_1}\right)^{\frac{1}{2}} - 1 \right\} \qquad 5\text{-}4$$

T_1 is an unknown quantity, but equation 5-4 can nevertheless be compared with experiment by noticing that

$$\left(\frac{T_m}{T_1}\right)^{\frac{1}{2}} - 1 \sim \left(\frac{T_m}{T_1}\right)^{\frac{1}{2}} \qquad 5\text{-}5$$

since T_m is of the order of KEV and T_1 is usually of the order of eV.

Hence, while σ cannot be calculated from equation 5-4, we can take a ratio of σ's for two different ions such as As and Ar bombarding the same iron-oxygen substrate. Then T_1 will cancel from the expression if equation 5-5 is employed. The results of this procedure are displayed in Table 4, where the experimental result and theoretical calculation are seen to agree to within 10%. This error is quite satisfactorily explained by experimental error and the errors inherent in using equation 5-3 for the collision cross-section. We also note that equations 5-2 and 5-4 can be combined to give an expression for which T_1 is the only unknown. The values of T_1 calculated in this way for the two bombarding ions are shown in Table 4. It can be seen that good agreement between the two calculated values is obtained, giving an average value of 24 eV for the minimum energy required to recoil implant an oxygen atom. It is significant that this number is similar in magnitude to the usual minimum energy to create a Frenkel pair determined in most solids.

In both the As^+ and the Ar^+ experiments at 65°K, the amount of oxygen present in the sample was approximately equal to the number of displaced iron atoms as calculated from the iron surface peak. This suggests that an iron oxide compound is forming, with stoichiometry FeO. This compound would result in an amorphous layer of iron oxide on the surface, thus explaining the observed spectra.

The above considerations concerning recoil implantation and oxide formation lead to several interesting conclusions about the mechanism of the proposed model. Firstly, we have assumed that for every oxygen atom which is recoil implanted, another oxygen atom from the environment immediately adsorbs on the target surface. This suggests that

vacancies, created by the recoils, migrate quickly to the surface of the target, where they are rapidly filled with oxygen from the environment. Secondly, we have assumed that an iron oxide compound is formed. Most of the collisions between the bombarding ion and the oxygen atoms of the surface oxide will be small angle low energy transfer collisions, resulting in the oxygen atom remaining in the oxide layer. In order for the oxide to continue to grow, there must be some mechanism which enhances diffusion of the oxygen recoils into the bulk crystal, where the proposed chemical reaction with Fe lattice atoms can take place.

As a general conclusion, we also note that if radiation damage to ion bombarded single crystal iron is to be effectively studied by the channeling technique, recoil implantation of impurities on the target surface must be avoided. This can be accomplished in iron at low temperatures if the cryo-shield surrounding the target is at $\sim$30°K.

5-2. Substitutional Fraction

Figure 16 shows the aligned <110> backscattered spectrum obtained from a single crystal of Fe implanted with several doses of 60 KEV As^+ at room temperature. Also shown are the aligned <110> spectrum obtained from the unimplanted sample and the non-aligned spectrum after implant. The unimplanted Fe spectrum verifies that there were no surface impurity peaks in the region corresponding to the As peak. Hence, the reduced yield under the As peak for the aligned spectrum following implant compared to the random spectrum represents As atoms which are shadowed by the <110> atomic rows.

There are three main difficulties in calculating the substitutional fraction of As in the Fe crystal lattice. Firstly, in the random spectrum,

there is some pulse pileup in the region of the As peak. In order to take this problem into account, a random spectrum was taken from an unimplanted sample with the same He^+ beam current. It is reasonable to assume that the pileup is the same in both cases, hence the two spectra are subtracted to obtain Y_R^{As}, the random yield from implanted As. The As yield from the aligned crystal's spectrum, Y_A^{As}, was assumed to have negligible pulse pileup.

A second difficulty can be inferred from an examination of Figure 16. Iron and arsenic are sufficiently close in atomic weight so that the detector resolution does not provide 100% separation in the backscattered spectrum. This problem was overcome by simply computing Y_A^{As} and Y_R^{As} from regions of the spectra for which there is no overlap of yields. This procedure introduces some error which is not considered to be serious, since the overlap is small. In Figure 16, channel 197 was chosen as the point where overlap starts to become significant.

The fraction of As shadowed by the rows, F_s, was determined using the relationship[19]

$$F_s = \frac{1 - \frac{Y_A^{As}}{Y_R^{As}}}{1 - \chi} \qquad 5\text{-}6$$

where $(1 - \chi)$ corrects for the fraction of the beam not channeled. The choice of χ represents the third difficulty of calculating F_s. Ideally, χ varies over the whole range of the implanted arsenic, but practically, this fact is difficult to apply. The mean range of 60 KEV As^+ in Fe was calculated[26] to be 145 Å. The value of χ at this depth represents an

average value for χ over the range of As, and was used to calculate F_s using equation 5-6.

The measurements were performed along both the <110> and <111> axes, and approximately the same F_s, $\sim.8(\pm.1)$, was obtained from each direction. Hence F_s represents the substitutional fraction. We also remark that approximately the same substitutional fraction was observed for both room temperature and 35°K experiments. At 65°K, the substitutional fraction was not determined, since the growth of surface oxide described in the previous section caused a much greater proportion of the As to appear non-substitutional. This is shown in Figure 17. Table 5 lists the results obtained from this work and that of others.

5-3. Radiation Damage

Figure 16 illustrates the characteristic features of backscattered spectra for heavy ion irradiated metals, i.e. the absence of a damage peak (as seen following bombardment of semi-conductors[29]) and a sigmoidal buildup[8] of dechanneled fraction across the damaged region. Figure 19 shows the damage vs. dose. The damage is a relative value, defined by:

$$\text{DAMAGE} = \frac{\frac{Y_D}{Y_R} - \chi}{1 - \chi} \qquad 5\text{-}7$$

where Y_D and Y_R are defined in Chapter 3, and χ is the normalized yield of the unimplanted crystal, measured at the same depth as Y_D. One important feature of Figure 19 is that the damage obtained from measuring the backscattered yield along the <110> direction is almost twice as high as the <111> direction, indicating an anisotropy in the damage distribution.

The (110) planes are the closest packed in the B.C.C. lattice, and hence would be the most susceptible to strain. This point possibly explains the observed anisotropy. Figure 19 also suggests that a saturation effect may be occurring at doses of about 10^{16} atoms/cm^2. This remains to be verified by further work. Also shown are results obtained from a 35°K implant, which indicate that the damage is greater for 300°K implants. At first this seems strange, since a high temperature implant should allow for greater annealing during and after the implant. This effect may be better understood with reference to Figure 20, which shows the back-scattered spectra from the <110> direction for almost equivalent doses of 60 KEV As^+ at 35°K and 300°K. Neglecting the surface peak, we see that the dechanneling behind the surface peak begins equivalently for both spectra. At ∿400 Å depth into the crystal, the low temperature spectrum changes slope, indicating an end to damage. The high temperature spectrum continues to rise at about the same slope until ∿600 Å depth, where it too changes slope. In Figure 21 the corresponding spectra from the unimplanted crystal have been substracted from both the low and high temperature spectra channel by channel, giving $\Delta\chi(t)$ vs. t, the distance into the crystal. This graph emphasizes where the dechanneling has become approximately constant and the damaged region has ended. We can conclude that the larger dechanneling in the 300°K case is due to the increased depth of damage, an effect which is thought to be caused by propagation of defects into the bulk sample at 300°K. This propagation phenomenon shall be discussed in more detail later.

The damage peaks observed in the spectra of Figure 20 offer an interesting comparison with similar work in semi-conductors. For semi-

conductors, the damage peak, attributed to direct backscatter from interstitials, usually implies greater or lesser radiation damage to the lattice in some proportion to its size. Larger damage peaks also produce greater dechanneling. From Figure 20 we observe that this is not the case in iron, where the low temperature damage peak is significantly larger than the high temperature damage peak, yet the sample irradiated at 300°K clearly shows greater dechanneling. A possible reason for the enhanced damage peak at 35°K can be determined by examining Figure 22, which shows the spectra of Figure 20 replotted with the surface peaks from the corresponding unimplanted spectrum substracted off channel by channel. The 300°K implant shows no evidence of any interstitial atoms, while the 35°K implant shows $\sim 3 \times 10^{15}$ Fe atoms/cm^2 in random locations as calculated from the remaining damage peak. It is thought that these displaced atoms are due to the oxygen recoil implantation effect described in section 5-1. An FeO layer of this magnitude would produce about 200 O^{16} counts spread over the detector resolution at about channel 90. This number constitutes less than the statistical error in the backscattered spectrum, and hence would not be visible.

From Table 3, we find that $N_d = 707$, where N_d is the number of displaced Fe atoms per incident 60 KEV As^+ ion. In semi-conductors, the measured number of displaced atoms per incident ion, N_d^*, has been 2-6 times the N_d predicted by equation 5-8.[29] N_d^* is determined in semi-conductors by dividing the total number of displaced atoms/cm^2, obtained from damage peak and utilizing equation 3-13, by the dose. In iron, this procedure would lead to an N_d^* several orders of magnitude smaller than N_d. Eisen and Bottiger[40] have pointed out that due to the tendency of

the channeled particle flux to peak near the centre of the channels (the flux peaking effect[41]), the channeling technique is considerably more sensitive to interstitials than atoms displaced slightly ($\sim$.1-.2 Å) from the row. It is the latter defect which result in the spectra of Figure 16. These defects produce strain fields in the crystal which increase dechanneling in the damaged region, but yield no damage peak, as caused by direct backscatter from interstitials in semi-conductors.

The depth scale of Figure 16 is calculated with the use of equation 3-10, using the stopping cross-section, S(E), for He^+ in Fe taken from Ziegler and Chu.[42] It should be pointed out that the stopping cross-section used was the value for random incidence. However, the stopping cross-section for an ingoing particle which is channeled may be considerably less. Precise values for channeled particles in Fe are not available, although measured values in Si[43] have indicated values of $\sim$0.6-0.8 of the random value, depending on the beam energy and the channel. Bottiger and Eisen[40] have recommended using the random value for damage measurement in Si. A value of .5 $S_{Random}(E)$, for a depth of 400 Å would only result in an inaccuracy of $\sim$25%.

Figure 23 shows the depth of damage parameters, X_D, vs. dose. As described in Chapter 3, X_D denotes the distance between the surface of the target (taken as the channel in the random spectrum whose yield is $\frac{1}{2}Y_R$), and the estimated end of the damaged region (the "knee" in the spectrum, as in Figure 10). It appears that the depth of damage increases almost linearly with dose for 300°K experiments. However, the low dose points may be significantly in error, since the channels are not sufficiently damaged to justify the use of the random stopping power for

channeled particles. We also note that the <111> points are consistently lower than the <110> points. The <111> channels have ∿1.6 times the cross-sectional area of the <110> channels, and are damaged less due to the observed anisotropy. Hence the <111> channels are expected to have smaller channeled particle stopping powers. This has been neglected in the analysis, lowering the <111> points on Figure 23.

Figure 24 shows the damage depth distribution caused by 60 KEV As^+ in Fe, calculated using a Monte Carlo technique.(44) It can be seen that the bulk of the damage will be deposited over approximately the first 300 Å. Figure 23 indicates that while the measurements at 35°K reasonably support this calculation, the damage for the 300°K high dose experiment is almost twice as deep. This observation leads to the conclusion that some mechanism exists which enables defects to propagate into the crystal at 300°K. This finding is consistent with the results of Gettings et al.(7) who observed anomalously deep damage in 300°K ion bombarded vanadium, and by Pronko in self-ion bombarded gold, as discussed in section 3-2-3.

However, Figure 21 also indicates that the rate of dechanneling with depth into the sample is approximately constant and equal for both the 300°K and 35°K <110> cases. This suggests that the damage created when defects propagate into the bulk crystal is very similar to the damage created by the ion bombardment. Also shown in Figure 21 is the <111> 35°K case, which shows the anisotropy in damage not only as a reduced yield, but also as a difference of slope, $d\chi/dt$, in the damaged region. For the <111> direction, $d\chi/dt = -1.32 \times 10^{-4}$ Å^{-1}, while for the <110> direction, $d\chi/dt = -2.57 \times 10^{-4}$ Å^{-1}.

It is possible to modify the channeled beam mean

transverse energy and hence the flux distribution along the channel by slight misalignment of the crystal. Such a procedure should enhance backscattering from atoms only slightly displaced from the atomic row. Figure 25 shows the backscattered yield obtained when the 1.0 MEV He^+ beam is misaligned $\sim.48\ \psi_c$ from the <110> axis of an iron sample implanted with $\sim 9.2 \times 10^{15}$ ions/cm^2 of 60 KEV As^+ at 35°K. It can be seen that the effect of misalignment is solely to increase the dechanneling of the analyzing beam. There is no indication of increased direct back-scattering between the channeled portion of the beam and atoms displaced slightly from the row. These results are consistent with the hypothesis that radiation damage to metals by ion bombardment is mostly lattice strain. This may be contrasted with recent work in semi-conductors,[29] where it was found that the measured damage in Si, GaAs and GaP at 50°K produced by 20-40 KEV He^+, N^+ and Zn^+ increases significantly when the analyzing beam is slightly misaligned.

The channeling technique provides a method for directly measuring the effects of annealing on the damaged crystal lattice. Figure 26 shows that 300°K annealing an iron lattice which has been bombarded with 2.3×10^{15} As atoms/cm^2 of 120 KEV As_2^+ at 35°K causes significant recovery of strain as shown by the decreased dechanneling yield over the whole spectrum. It should be noted that the anneal consisted of slowly warming the sample to room temperature over a 15 minute period, and then recooling it to 35°K over a 30 minute period. It is known[45] that Fe has several recovery stages over this temperature range.

An interesting feature of molecular arsenic implants in iron at 35°K can be inferred from Figure 19, which shows the damage vs. dose. Firstly, it can be seen that the magnitude of the damage for the low dose

molecular implant at 35°K is just slightly less than the damage for the high dose atomic implant at 35°K. Also, Figure 23 shows that the damage extends over approximately the same depth. It appears, then, that the increased energy density of the molecular over the atomic implant (see Figure 6) has resulted in greater damage levels. This contrasts with recent work in Vanadium,[7] where the energy density had little effect on observed damage levels. We point out, however, that our results are tentative. Proof of this energy density effect should come from equivalent doses of atoms/cm^2, where direct comparison may be made.

Another interesting result is the significant decrease in the damage after the anneal described above. This result suggests that the proposed mechanism of defect propagation into the bulk crystal may depend on the implant itself (e.g. bombardment induced defect diffusion). Otherwise it would be expected that the anneal would increase the damage by allowing the defects to propagate deeper into the crystal. Also, the mechanism obviously depends on temperature and lattice properties, and may also depend on dose rate, metallurgical effects due to the implanted impurity, and total defect density.

6. CONCLUSIONS

1. At doses of $\sim 10^{16}$ ions/cm^2, 60 KEV As^+ ions were found to be 80(±10)% substitutional in the Fe single crystal lattice at both 300°K and 35°K.

2. Adsorption of oxygen on the sample surface from the vacuum environment and subsequent recoil implantation of this oxygen into the crystal during ion bombardment is found to have severe effects on the Rutherford backscattered spectrum. It is thought that vacancies, created when an oxygen atom is recoil implanted, migrate quickly to the target surface and are filled by another oxygen atom from the environment. This model accounts satisfactorily for the amount of oxygen observed in the crystal after ion bombardment. It is clear that this effect must be avoided if radiation damage produced in iron by ion bombardment is to be effectively studied.

3. A one to one correspondence is found between implanted oxygen atoms and displaced iron atoms. This suggests that a chemical compound is being formed, which in turn suggests that recoil implanted oxygen can migrate deeper into the sample.

4. When the implantation is performed at room temperature, the measured damage extends far deeper into the crystal than is expected. It is thought that this is due to a mechanism of defect diffusion. When the implantation is performed at 35°K, the damage depth agrees reasonably

with calculated values.

5. The damage is found to be of the kind that produces dechanneling of the analyzing beam, but not direct backscatter from interstitials. It is expected that the defects may be mostly in the form of lattice strain. The damage produced at 35°K and 300°K appears to be similar, but the amount is considerably higher in the latter case due to the defect diffusion mechanism postulated above. It is tentatively thought that bombardment with the same dose (in atoms/cm^2) of molecular arsenic (As_2^+) yields higher damage levels than the atomic (As^+) case. More work is needed for confirmation of this effect.

7. SUGGESTIONS FOR FURTHER WORK

This study has concerned itself primarily with 60 KEV As^+ bombardment of Fe at various doses and temperatures. This basic work can continue in order to obtain more data in the dose region (10^{15}-$10^{16}/cm^2$) studied, as well as extending the results to lower and higher doses, which would yield useful information on saturation and defect diffusion effects. Such work can continue in conjunction with annealing studies, impurity substitutional fraction studies, and studies of the effects on Fe lattice damage of different sample temperatures during irradiation and analysis. This work may also be directed towards verifying the effects energy density on damage, and determining the important functional parameters which govern the defect propagation mechanism.

Since an understanding of dechanneling is so important for interpreting the results of channeling measurements in metals, it is suggested that experiments designed to exclusively study dechanneling be undertaken. A fruitful beginning to this type of work may be a study on the effects of the choice of analyzing beam and its energy on dechanneling in unimplanted and damaged crystals.

As a final suggestion, alternate methods of sample preparation should be investigated to reduce the χ_{min} value for the unimplanted sample.

8. TABLES

TABLE 1. Various experimental and theoretical parameters for single crystal iron. Calculations are based on the theory of Barrett[17].

Parameter	Crystal Direction	Temperature °K	Experimental Value (this work)*	Experimental Value (ref. 2)†	Semi-Empirical Value* (ref. 17)
χ_{min}	<110>	300	∿ .045	.054	.032
χ_{min}	<110>	35	∿ .04	-	.014
χ_{min}	<111>	300	∿ .035	.028	.019
χ_{min}	<111>	35	∿ .034	-	.0077
$\psi_{1/2}$	<110>	35	-	-	.89°
$\psi_{1/2}$	<110>	35	∿1.03°	-	1.05°
$\psi_{1/2}$	<111>	300	-	-	1.1°
$\psi_{1/2}$	<111>	35	-	-	1.3°

*Channeling probe - 1.0 MEV He^+.

†Channeling probe - 2.0 MEV He^+.

TABLE 2. Substitutional fraction of Xe for various doses in single crystal iron. From Feldman and Murnick.[19]

Xe dose	Concentration at.%	Channel	Xe backscatter yield	Substitutional fraction
1×10^{14}	0.08	⟨110⟩	0.67 ± 0.20	0.39 ± 0.15
		⟨100⟩	0.59 ± 0.19	
1×10^{14}	0.13	⟨111⟩	0.69 ± 0.13	0.32 ± 0.15
		⟨110⟩	0.67 ± 0.20	
2.3×10^{14}	0.31	⟨111⟩	0.52 ± 0.06	0.49 ± 0.05
		⟨100⟩	0.49 ± 0.06	
2.3×10^{14}	Post-450 °C anneal	⟨111⟩	0.95 ± 0.05	0.09 ± 0.05
		⟨100⟩	0.88 ± 0.05	
2.5×10^{14}	0.34	⟨100⟩	0.53 ± 0.10	0.47 ± 0.10
3.8×10^{14}	0.51	⟨111⟩	0.59 ± 0.11	0.45 ± 0.10
		⟨100⟩	0.55 ± 0.12	
1×10^{16}	8.4	⟨111⟩	0.80 ± 0.03	
		⟨110⟩	0.87 ± 0.03	0.16 ± 0.03
		⟨100⟩	0.84 ± 0.03	

TABLE 3. Calculations on collision cascades for various ion-target pairs at various energies.

Ion	Fe^+ ref. 22	Fe^+	Ge^+ ref. 22	Ge^+	Kr^+ ref. 22	Kr^+	Xe^+ ref. 22	Xe^+	W^+ ref. 22	W^+	As^+	As_2^+	Ar^+	Ga^+	Bi^+	Ar^+
Target	Fe	Fe	Fe	Fe	Fe	Fe	Fe	Fe	Fe	Fe	Fe	Fe	Fe	V	V	Nb
Ion Energy (KEV)	80	80	80	80	80	80	80	80	80	80	60	120	60	150	300	300
No. of Vacancies in Cascade	507	878	513	914	518	927	535	962	548	984	707	1413	641			
$\nu(E)/E$		.627		.653		.662		.687		.703	.673	.673	.610	.599	.634	.451
$\langle X_D \rangle$ Å	193	169	169	147	156	135	105	104	95	90	114	114	179	329	299	1002
$\langle \Delta X_D^2 \rangle^{\frac{1}{2}}$ Å	120	100	102	87	96	80	64	62	59	53	68	68	107	190	176	564
$\langle Y_D^2 \rangle^{\frac{1}{2}}$ Å	77	65	65	57	60	52	44	40	40	34	46	46	72	118	106	405
θ_o eV/atom	.21	.089	.37	.14	.42	.18	1.26	.41	1.81	.69	.21	.42	.049	.030	.085	.0017

TABLE 4. Results from oxygen recoil implantation. ϕ_o is the ion dose, $N_o(\phi)$ is the number of ^{16}O atoms/cm^2.

Ion	Energy (KEV)	ε (ion → ^{16}O)	ϕ_o $\frac{\text{ions}}{\text{cm}^2}$ x 10^{15}	$N_o(o)$ $\frac{\text{atoms}}{\text{cm}^2}$ x 10^{16}	$N_o(\phi)$ $\frac{\text{atoms}}{\text{cm}^2}$ x 10^{16}	T_1 (eV)	$\frac{\sigma(As \rightarrow O)}{\sigma(Ar \rightarrow O)}$ Experimental	$\frac{\sigma(As \rightarrow O)}{\sigma(Ar \rightarrow O)}$ Theoretical
As^+	60	.3439	9.9	1.5±.1	7.58	25.6	2.01±.2	2.22
Ar^+	64	1.2311	9.8	1.5±.1	3.33	21.3		

TABLE 5. Summary of channeling information in the substitutional fraction of various impurities in iron.

Impurity	Dose atoms/cm^2	Implantation Energy (KEV)	Approximate Substitutional Fraction	Reference
Lu	$3x10^{15}$	40	0.40	38
Sr	$2x10^{16}$	150	0.85	36
Yb	10^{15}	60	0.5	39
Xe	10^{14}-10^{16}	100-200	0.45	19
Pb	$2x10^{14}$	100	0.82	19
Bi	$2x10^{14}$	100	0.79	19
Tl	$2x10^{14}$	170	0.84	19
As	$9x10^{15}$	60	0.8±0.1	This Work

9. FIGURES

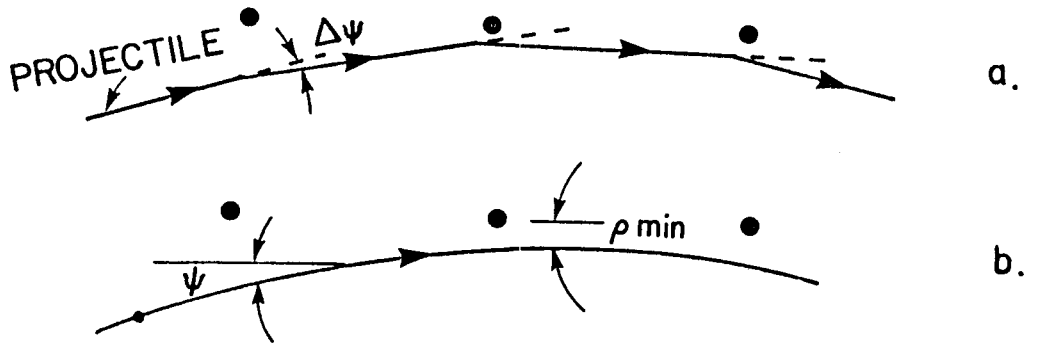

FIGURE 1a. The impulse model of channeling.

1b. The continuum model of channeling.

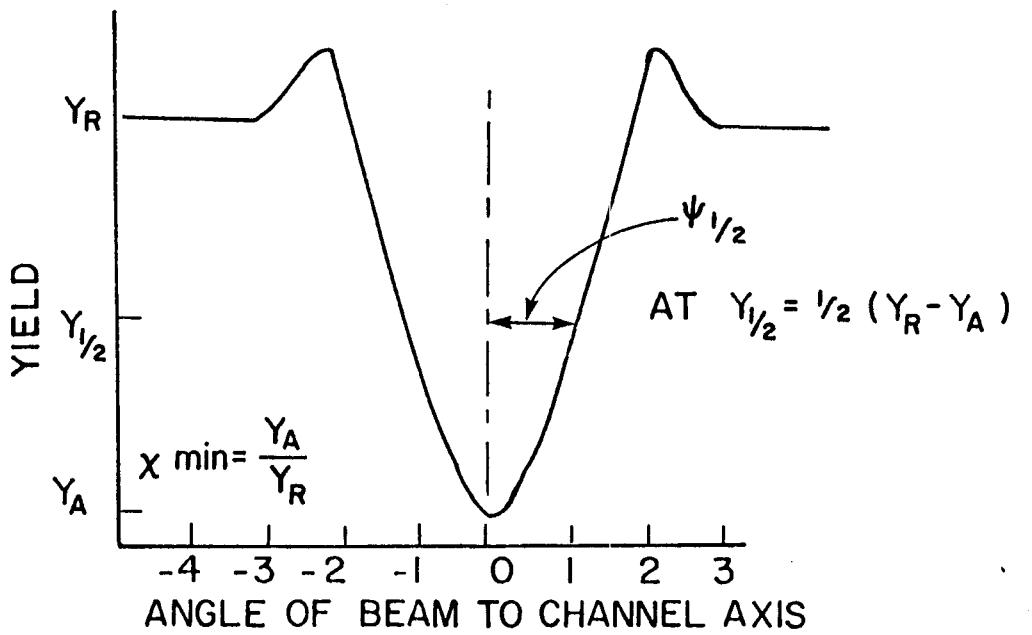

FIGURE 2. The form of a Rutherford backscattered yield for an angular scan of a major crystallographic axis.

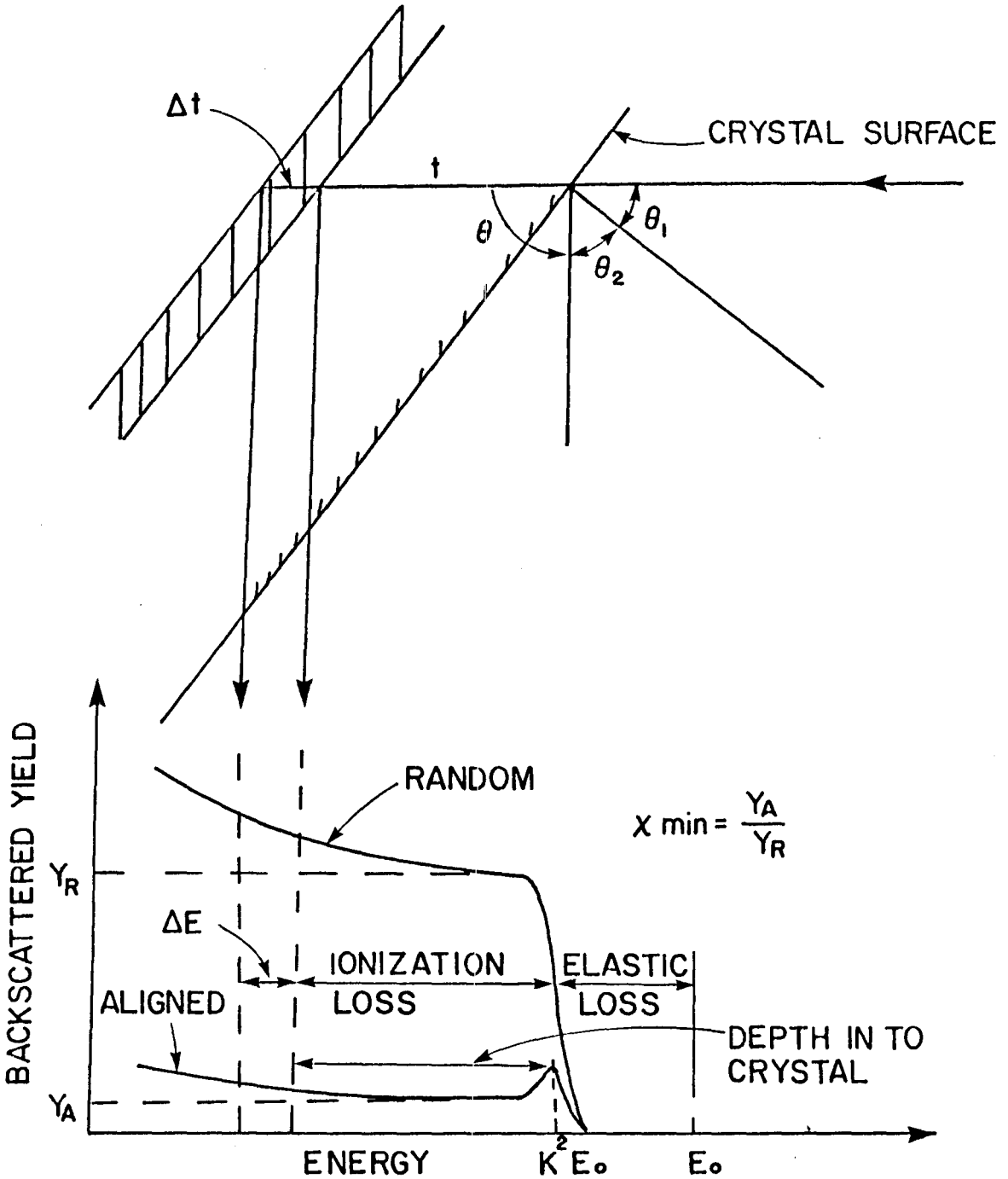

FIGURE 3. Principles of elastic scattering experiment.

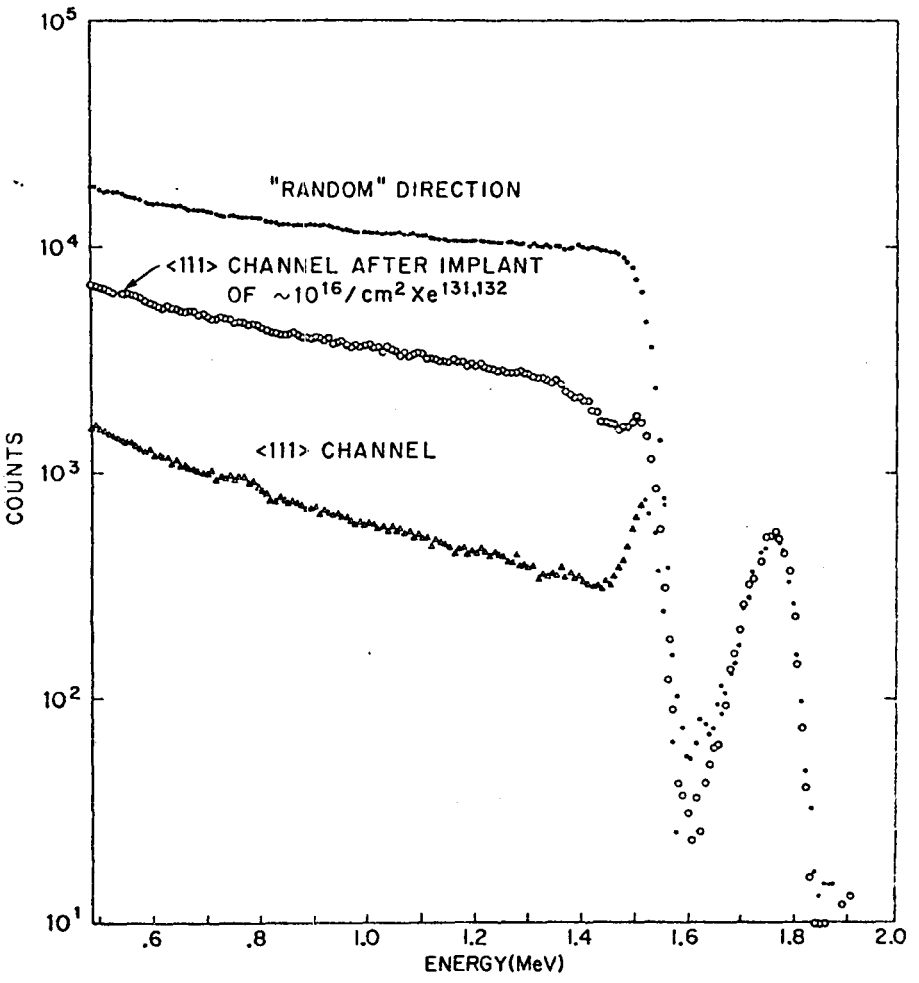

FIGURE 4. Normalized backscattered 2.0 MEV He^+ spectra pre- and post-high-dose implant of 200 KEV Xe into iron crystal. From Feldman and Murnick.[19]

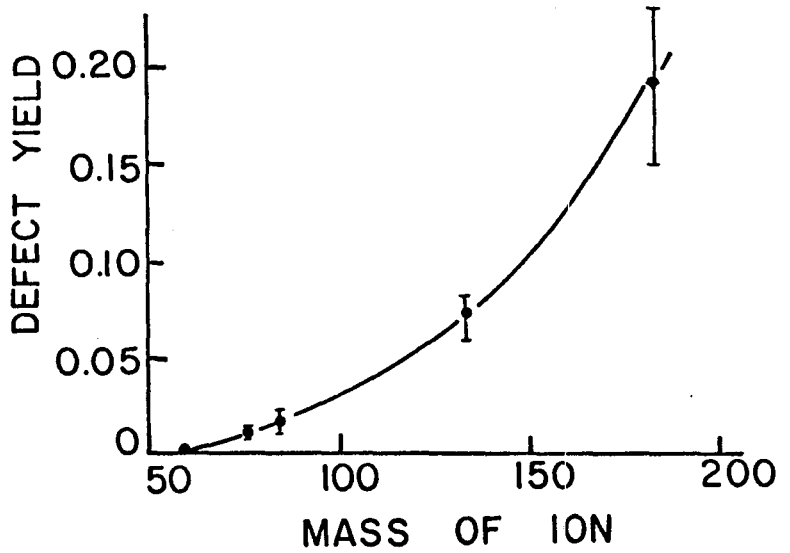

FIGURE 5. Plot of defect yield as a function of mass. Ion energies were all 80 KEV and doses were $5x10^{12}$ ions/cm^2. From English et al.[22]

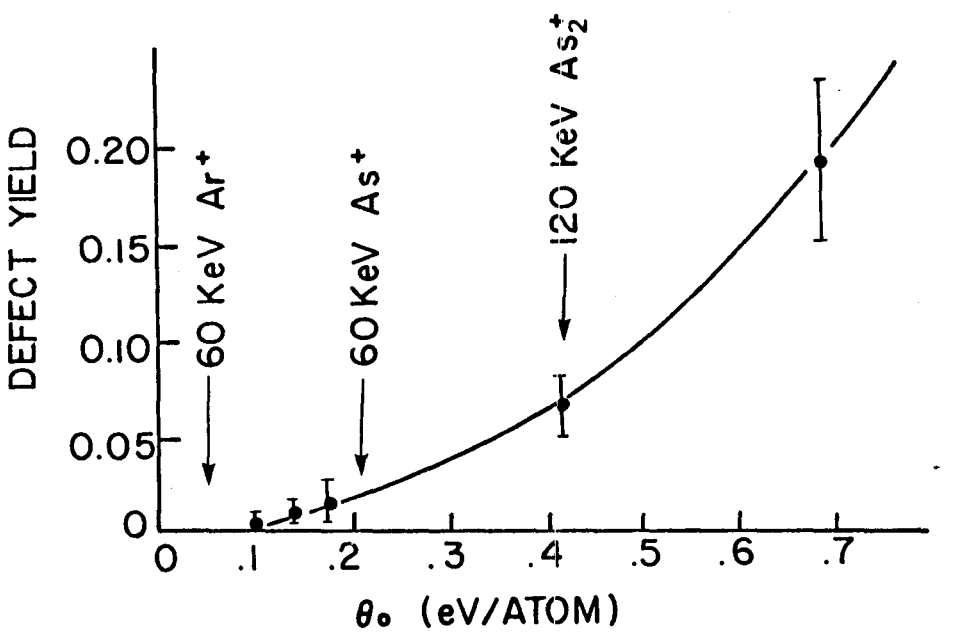

FIGURE 6. Plot of defect yield vs. maximum energy density in the cascade. Values are obtained from Table 3 and Figure 5.

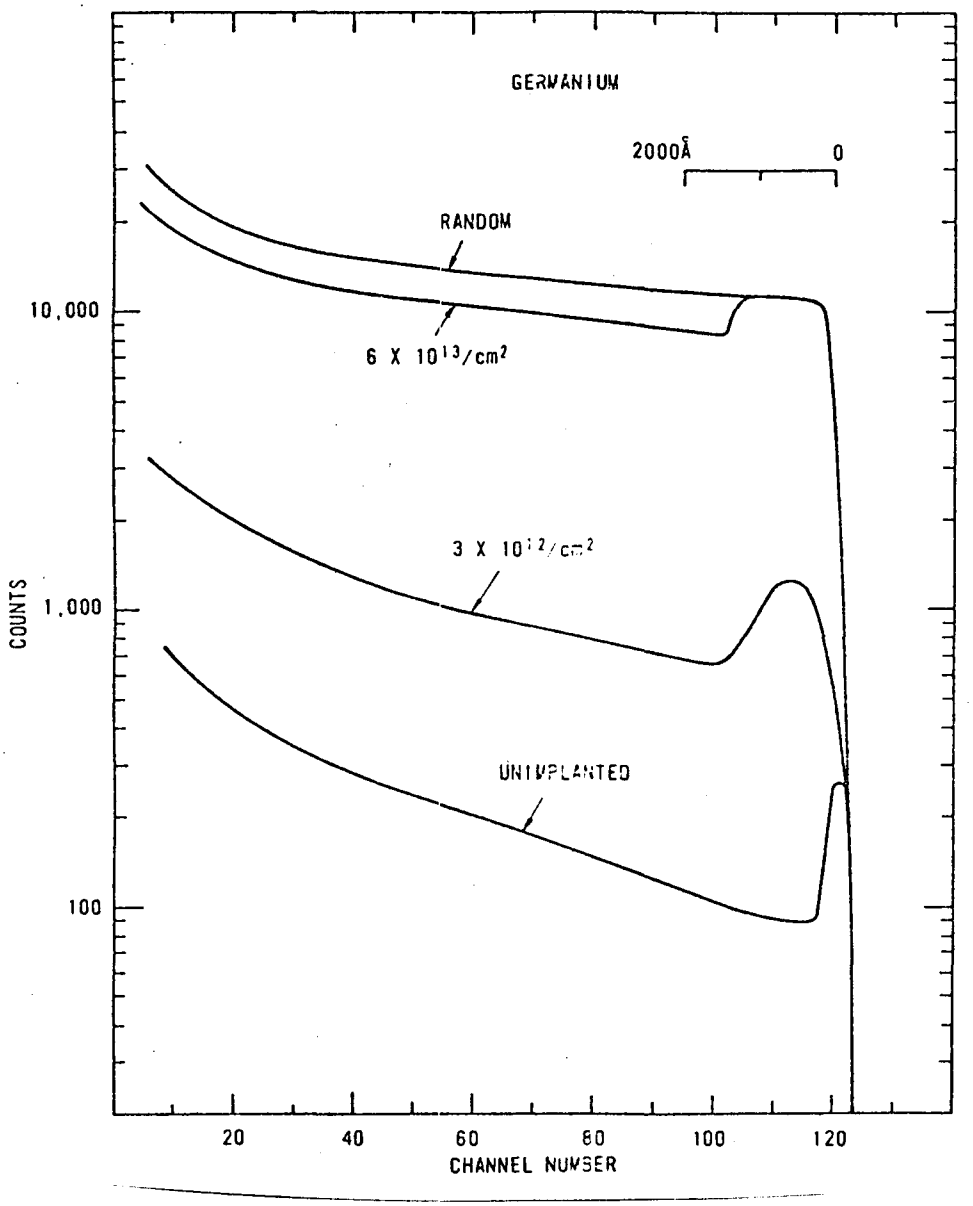

FIGURE 7. Backscattered energy spectra of 1.5 MEV He^+ ions from aligned <110> germanium crystals implanted at 25°K with various fluences of 300 KEV Ar^+ ions. From Pronko et al.[30]

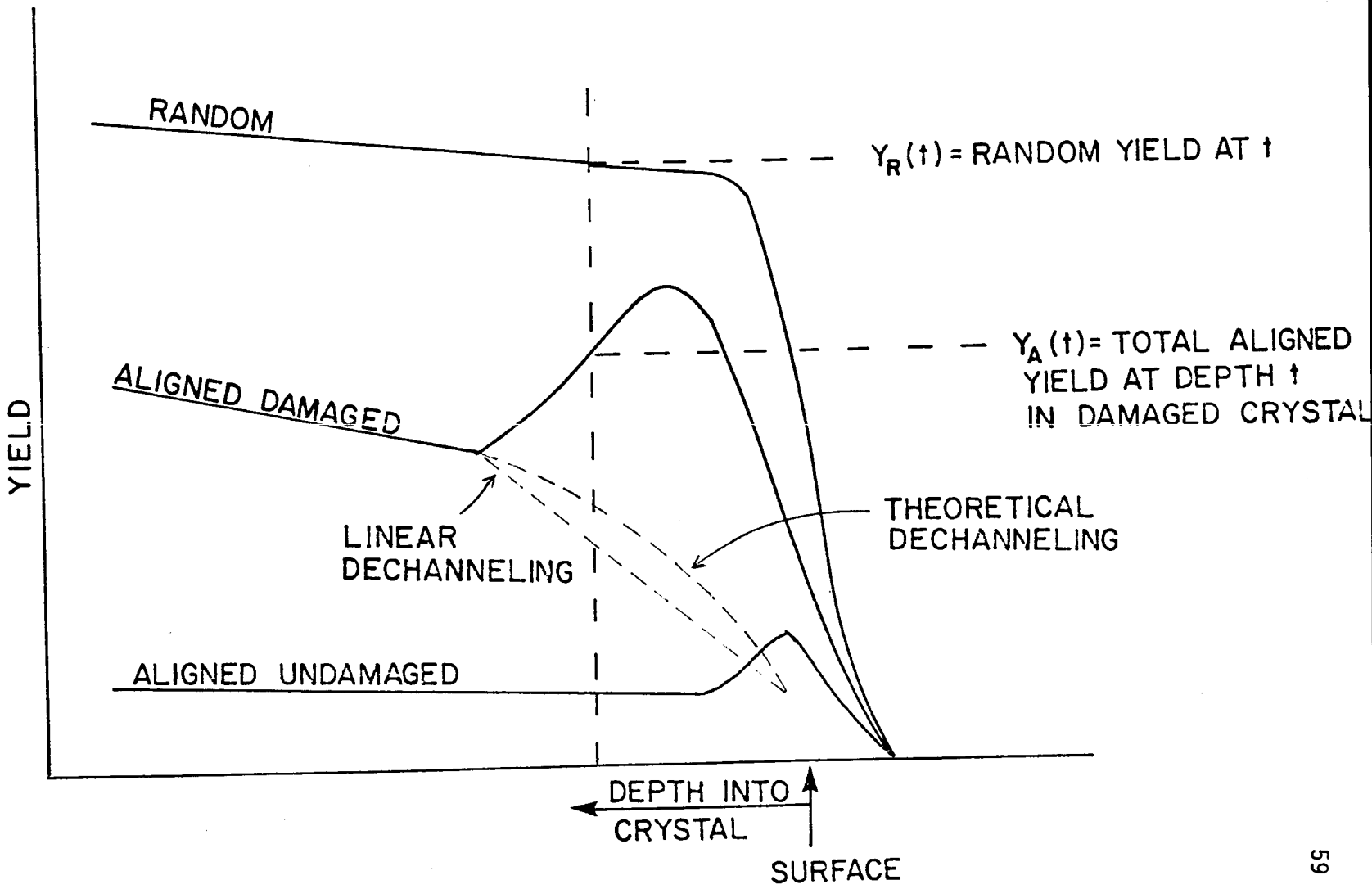

FIGURE 8. Rutherford backscatter yields for a typical semi-conductor. The theoretical dechanneling curve may be calculated using single, plural, or multiple scatter dechanneling.

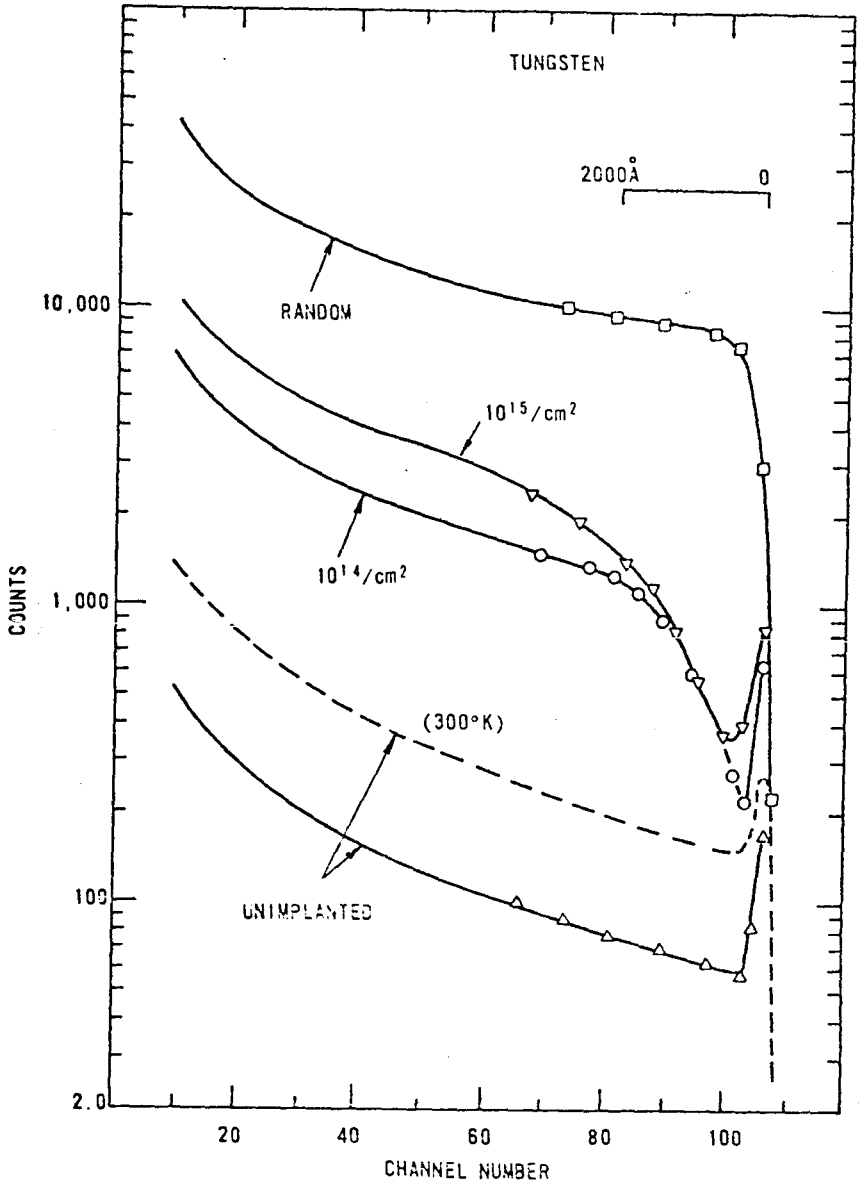

FIGURE 9a. Backscattered energy spectra of 1.5 MEV He^+ ions from aligned <110> Tungsten implanted at 25°K with various fluences of 300 KEV Ar^+.

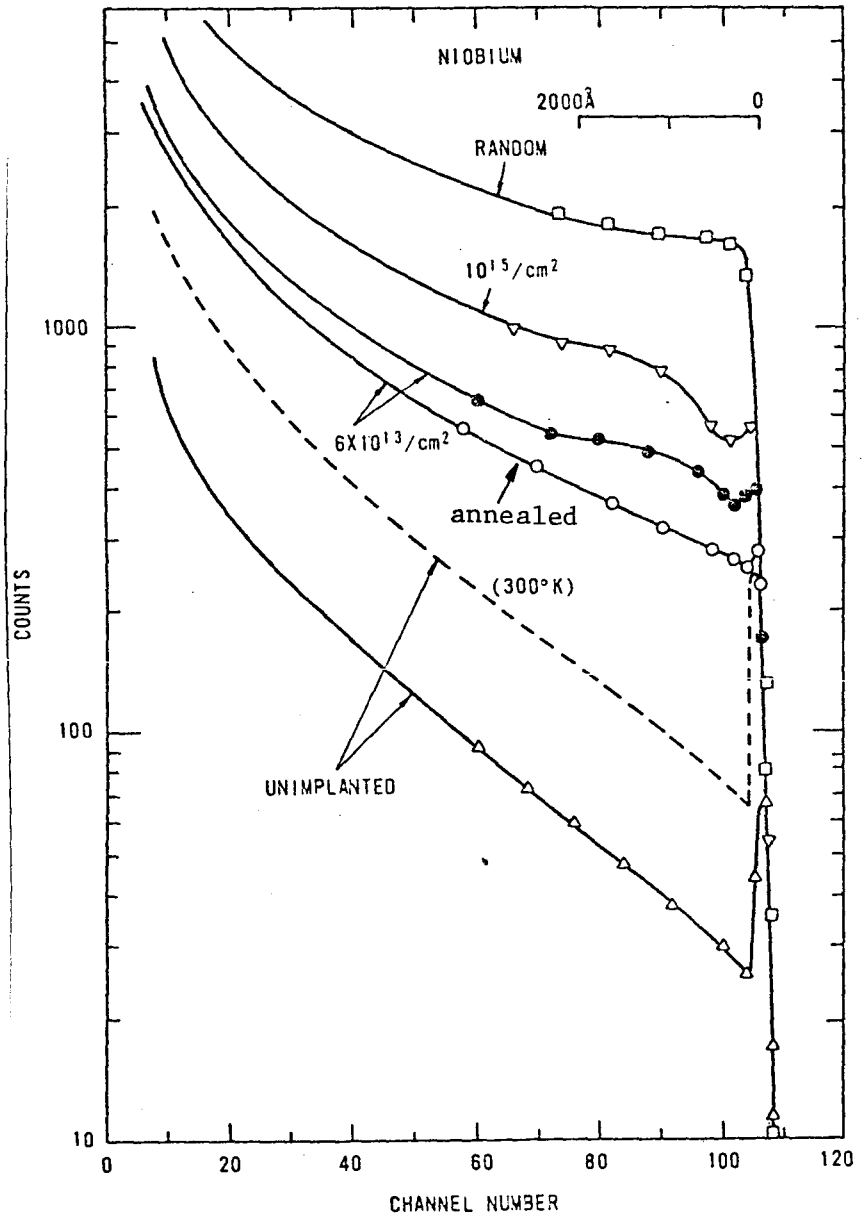

FIGURE 9b. Same, but with 1.0 MEV He^+ ions from aligned <100> niobium. From Pronko et al.[30]

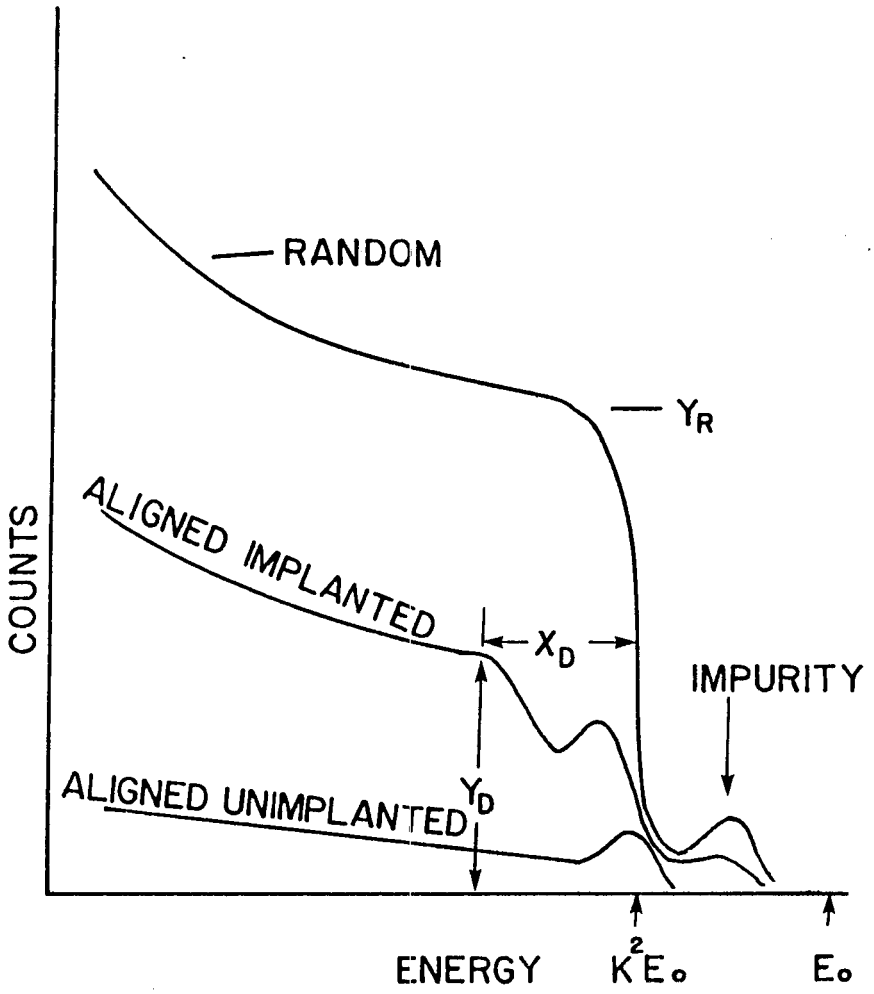

FIGURE 10. Idealized backscattering spectrum for metal showing parameters used to define amount and depth of disorder. From Gettings et al.[7]

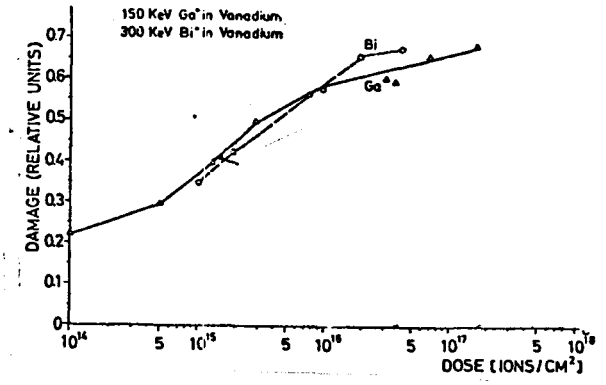

FIGURE 11. The damage (Y_D/Y_R, as defined in the text) dependence on implanted ion dose for 150 KEV Ga^+ and 300 KEV Bi^+ ions. From Gettings et al.(7)

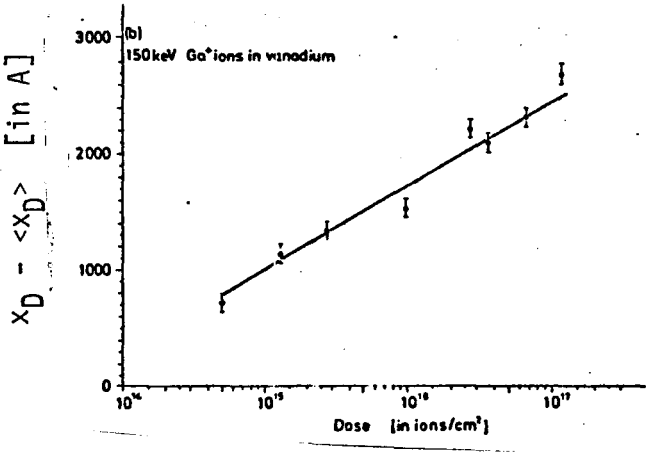

FIGURE 12. Variation of the depth of damage, X_D (minus the projected range) as a function of dose for 150 KEV Ga^+ implanted in Vanadium. From Gettings et al.(7)

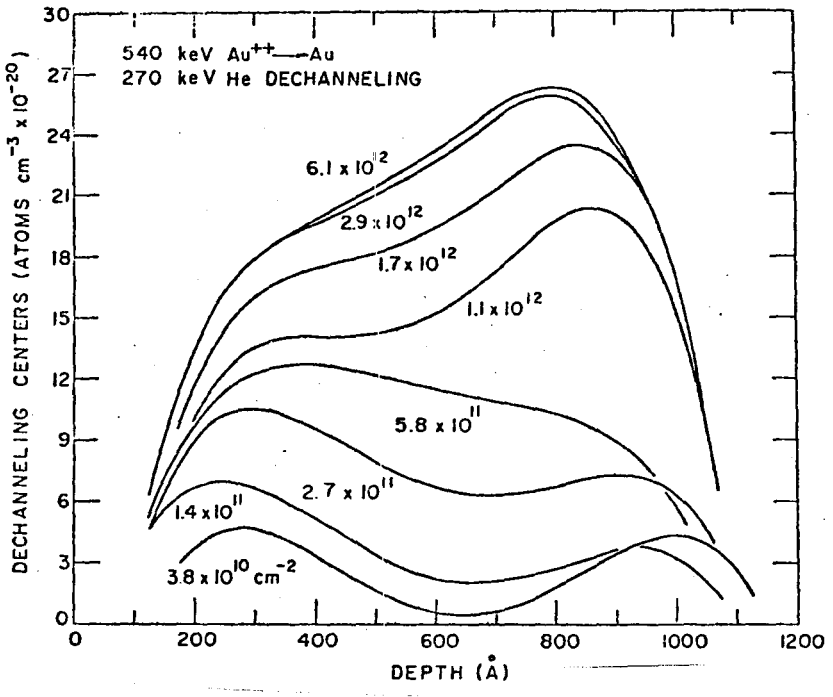

FIGURE 13. Defect distributions obtained with equation 3-14 for .27 MEV He^+ dechanneling in 1200 Å single-crystal gold film after 540 KEV self-ion irradiation to the fluences indicated. From Pronko.[8]

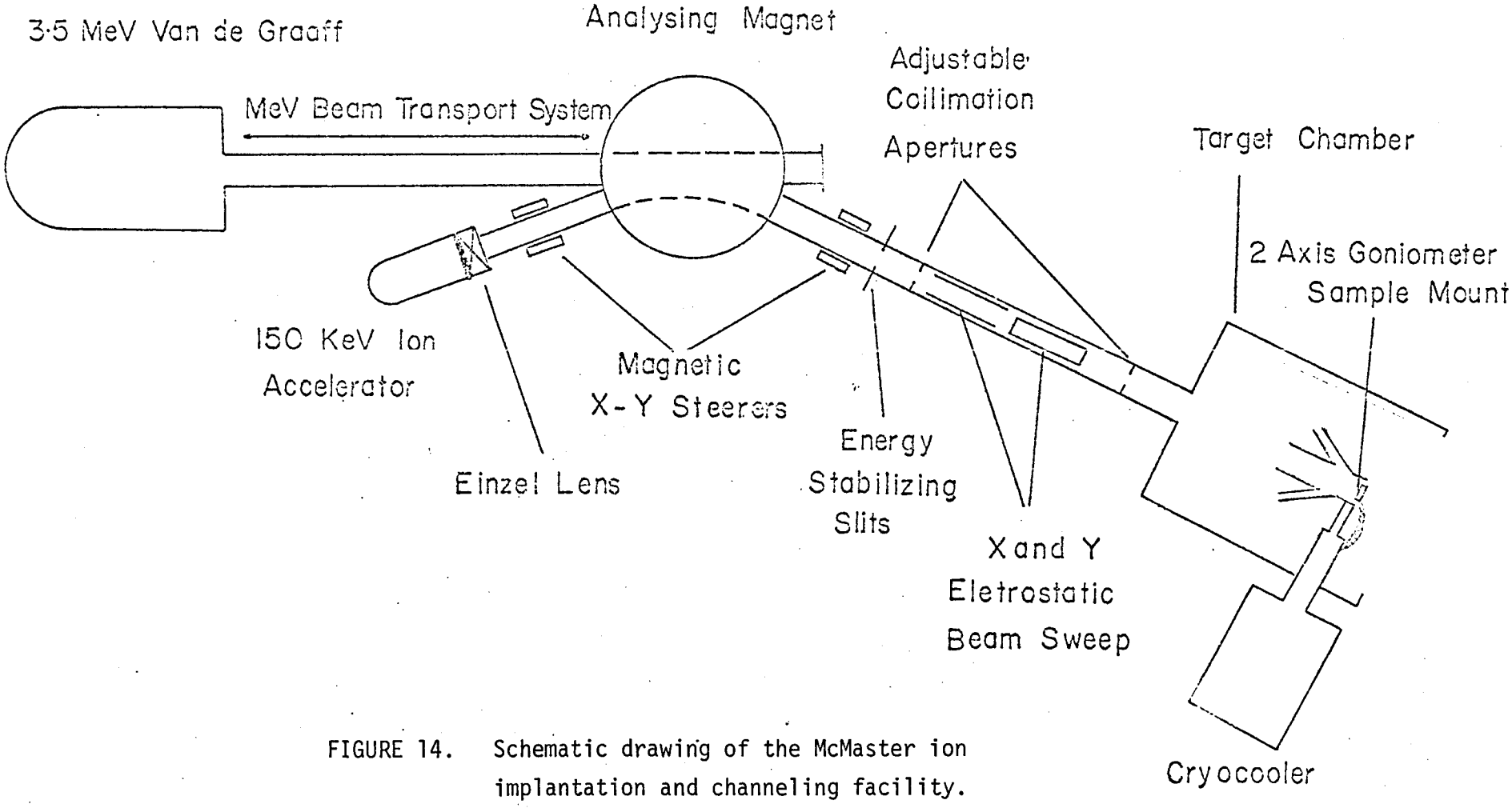

FIGURE 14. Schematic drawing of the McMaster ion implantation and channeling facility.

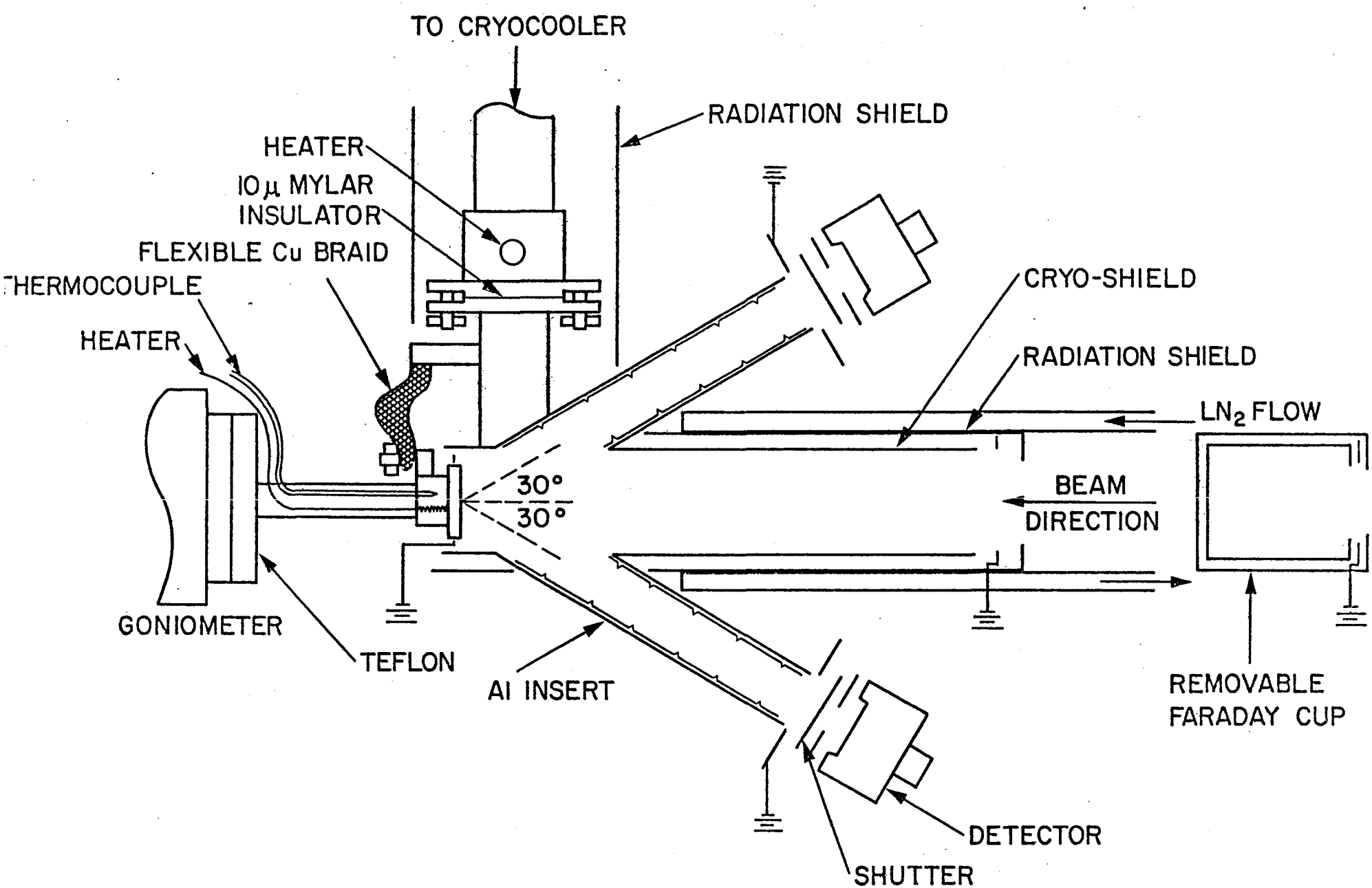

FIGURE 15. Schematic drawing of target chamber.

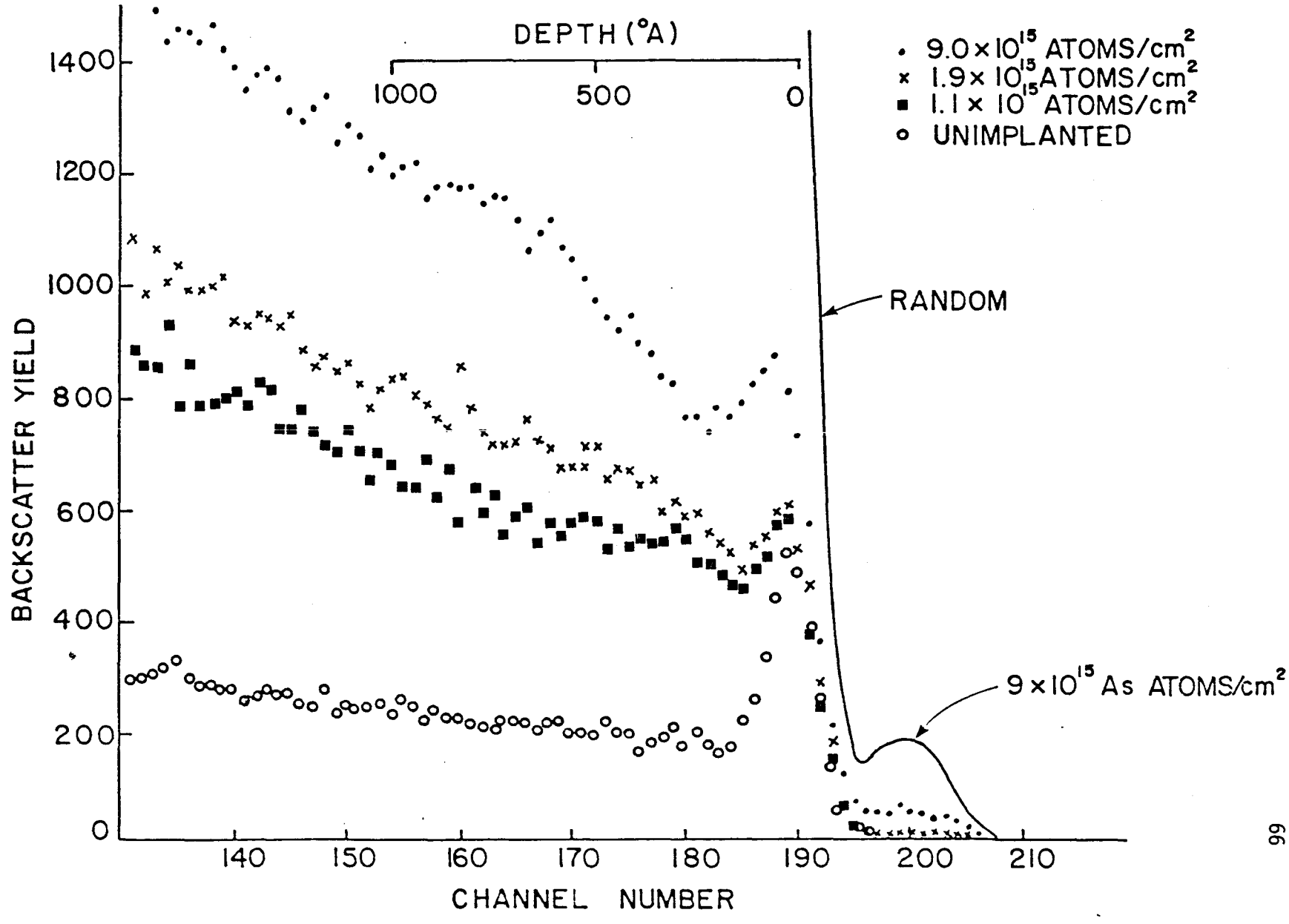

FIGURE 16. Backscattered spectra from Fe along the <110> direction for 60 KEV As^+ implanted and analyzed at room temperature.

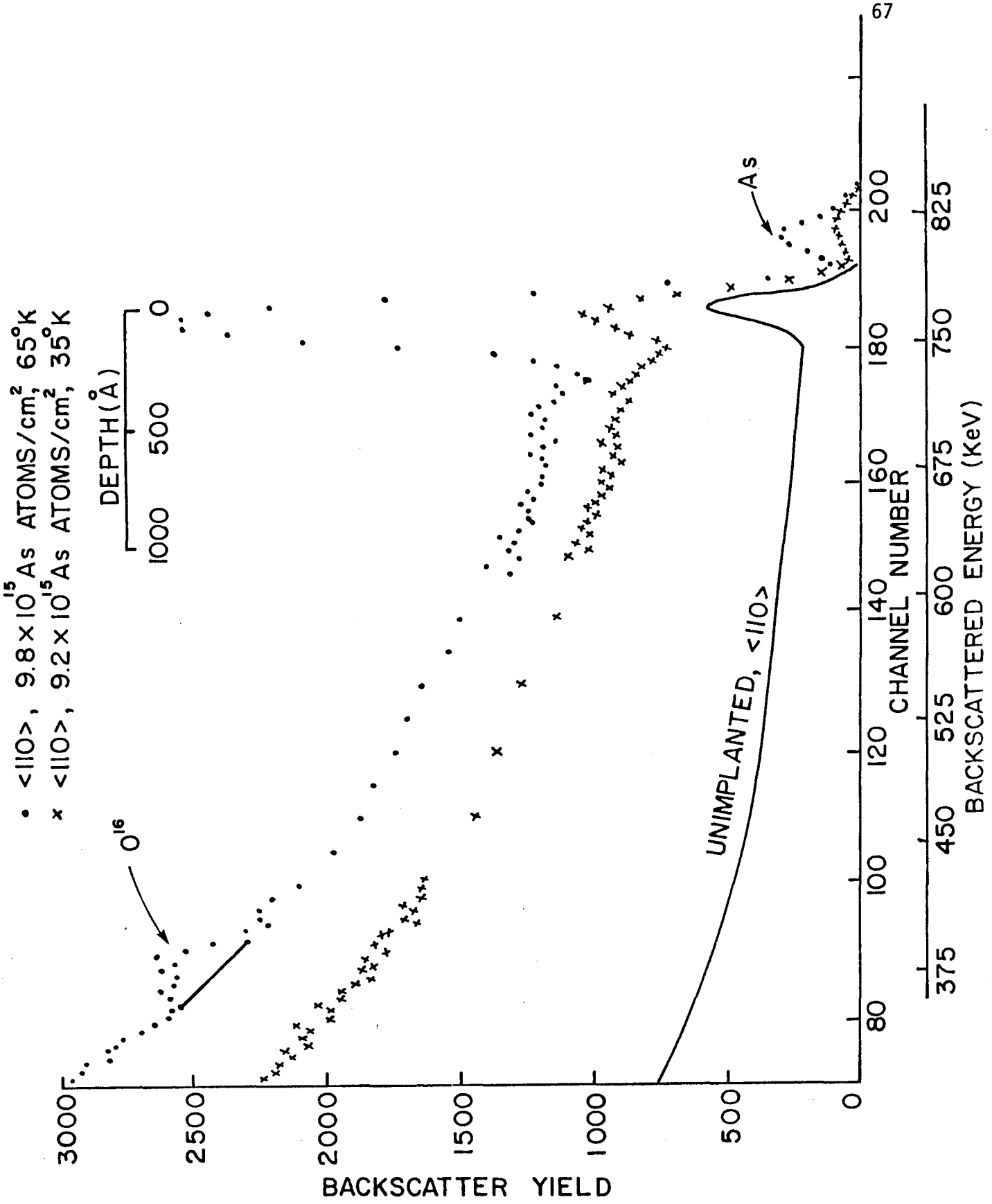

FIGURE 17. Backscattered yield showing the effects of performing 60 KEV As^+ implants at 65°K and 35°K.

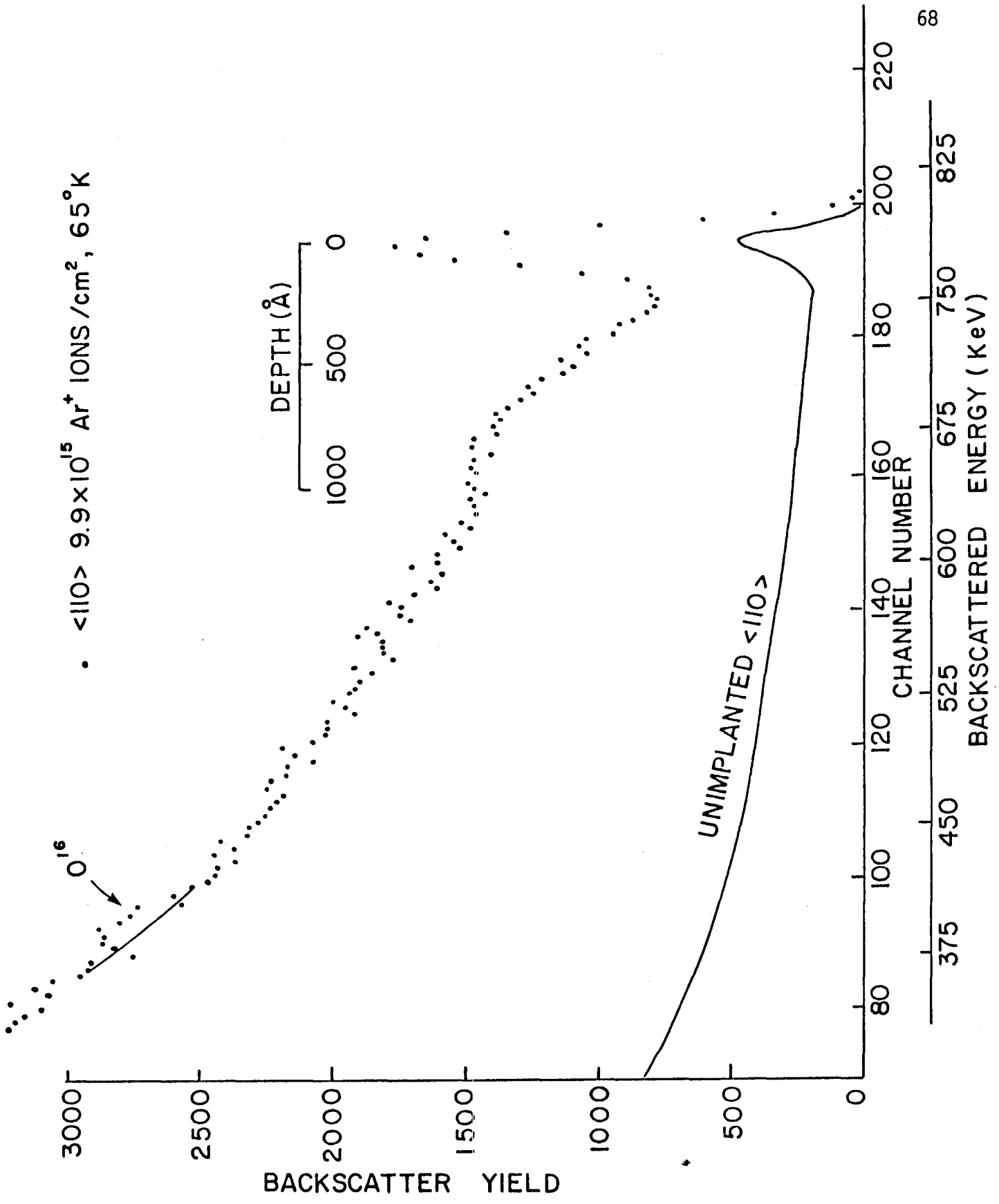

FIGURE 18. Backscattered yield showing the effects of performing 64 KEV Ar^+ implants at 65°K.

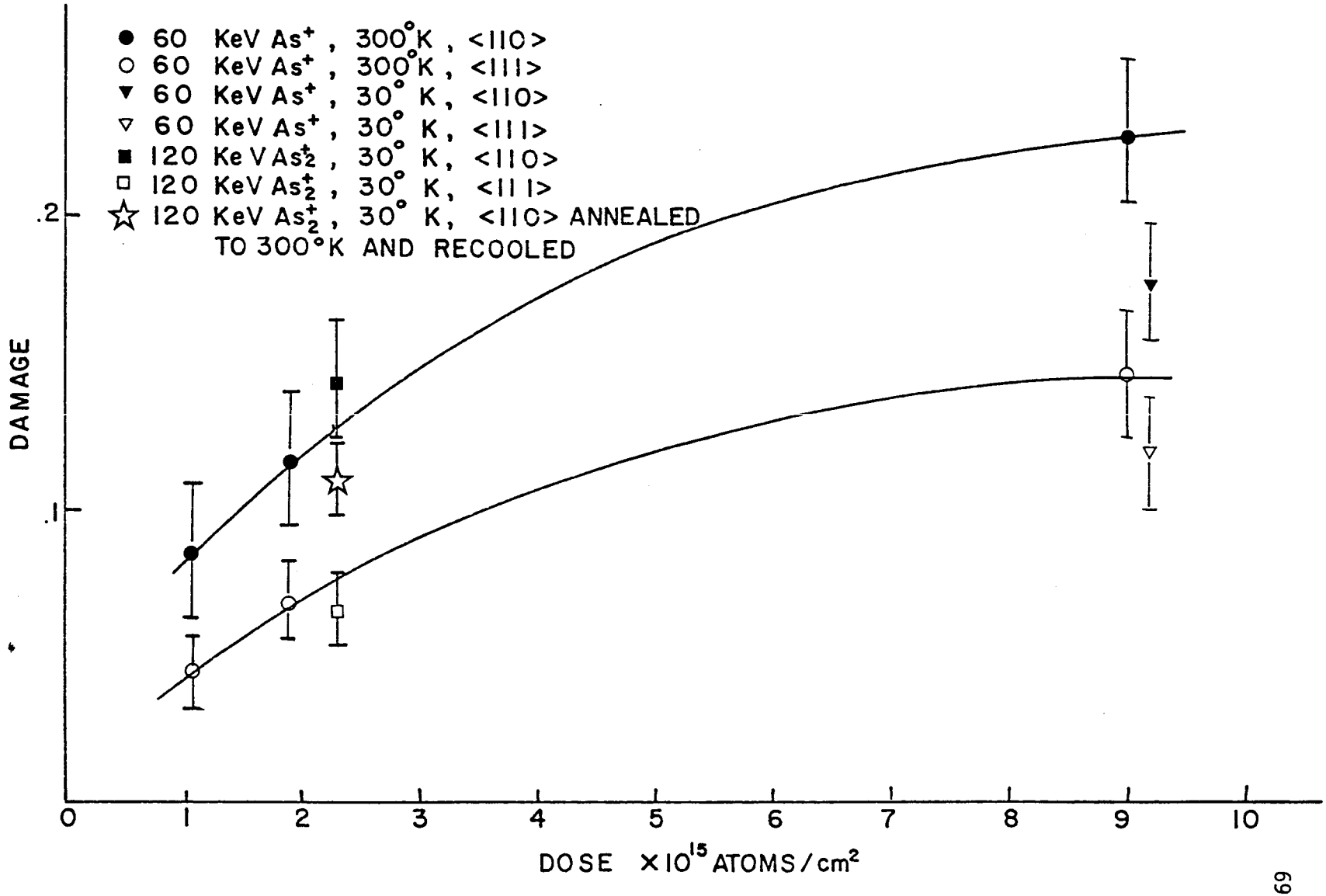

FIGURE 19. The damage vs. dose for various ions, energies, and temperatures.

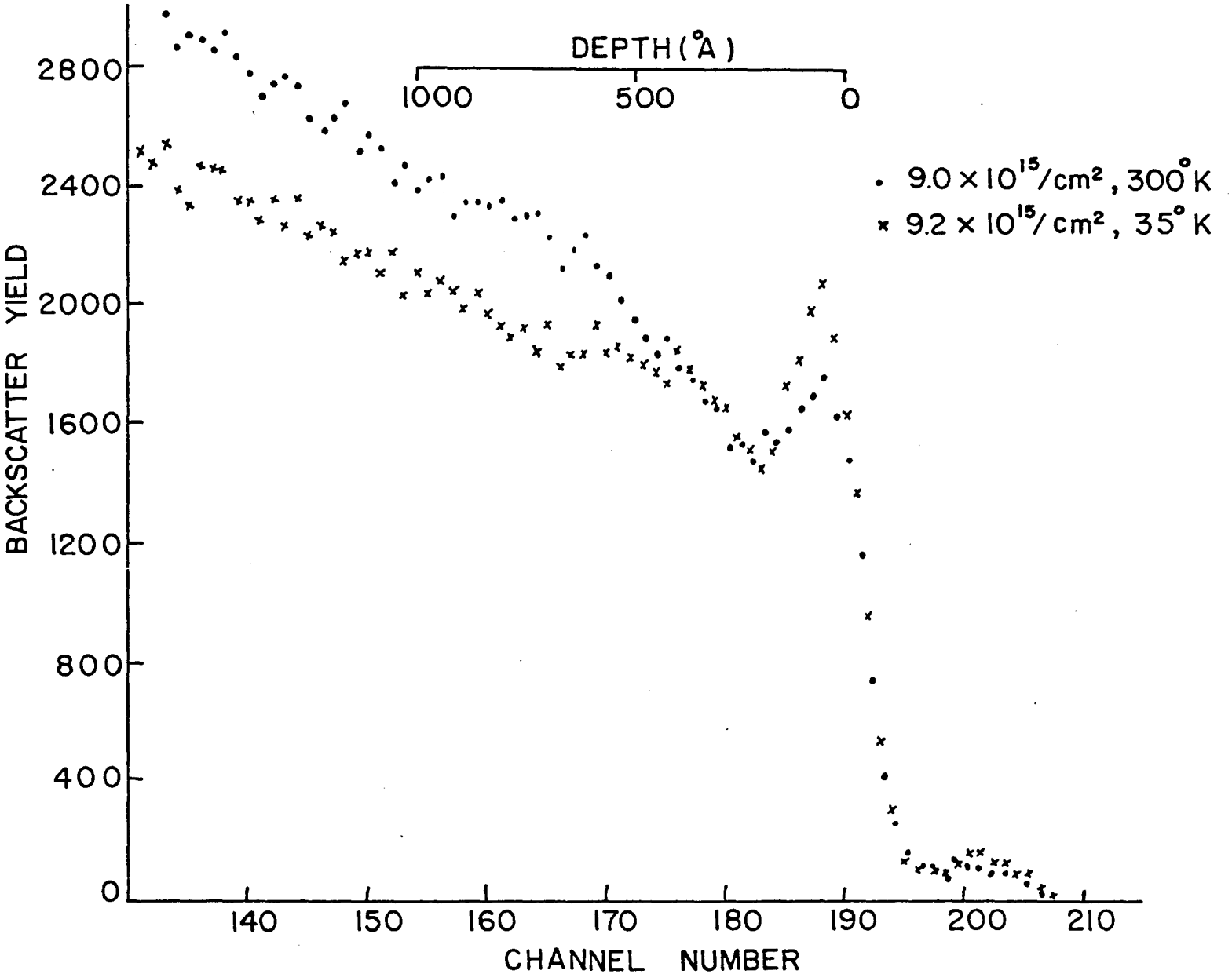

FIGURE 20. Backscattered spectra along <110> direction for 60 KEV As^+ implanted at room temperature and 35°K. The analysis was performed with 1.0 MEV He^+, with the sample held at the same temperature as during the implant.

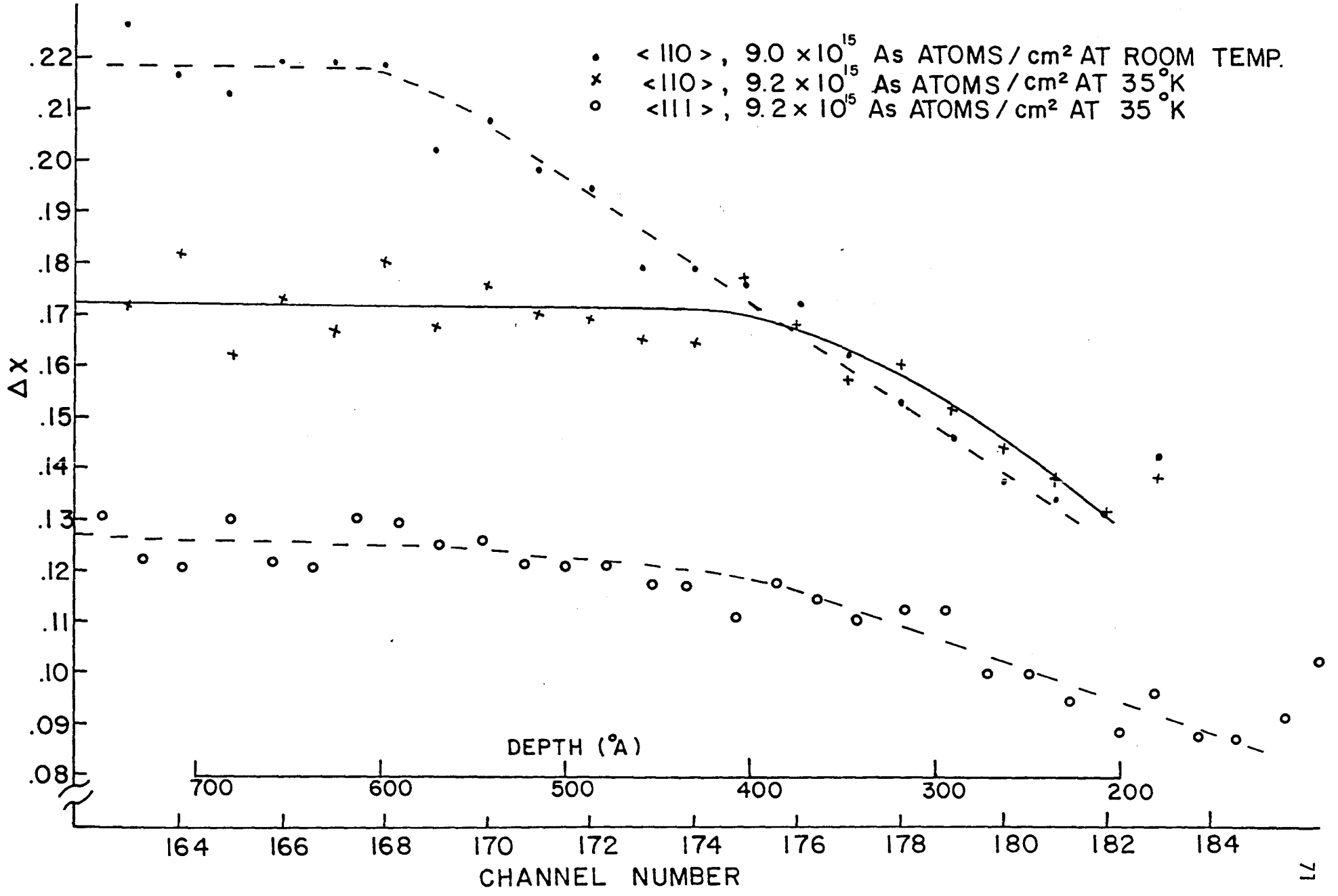

FIGURE 21. The change in normalized yield, channel by channel, vs. depth into the crystal.

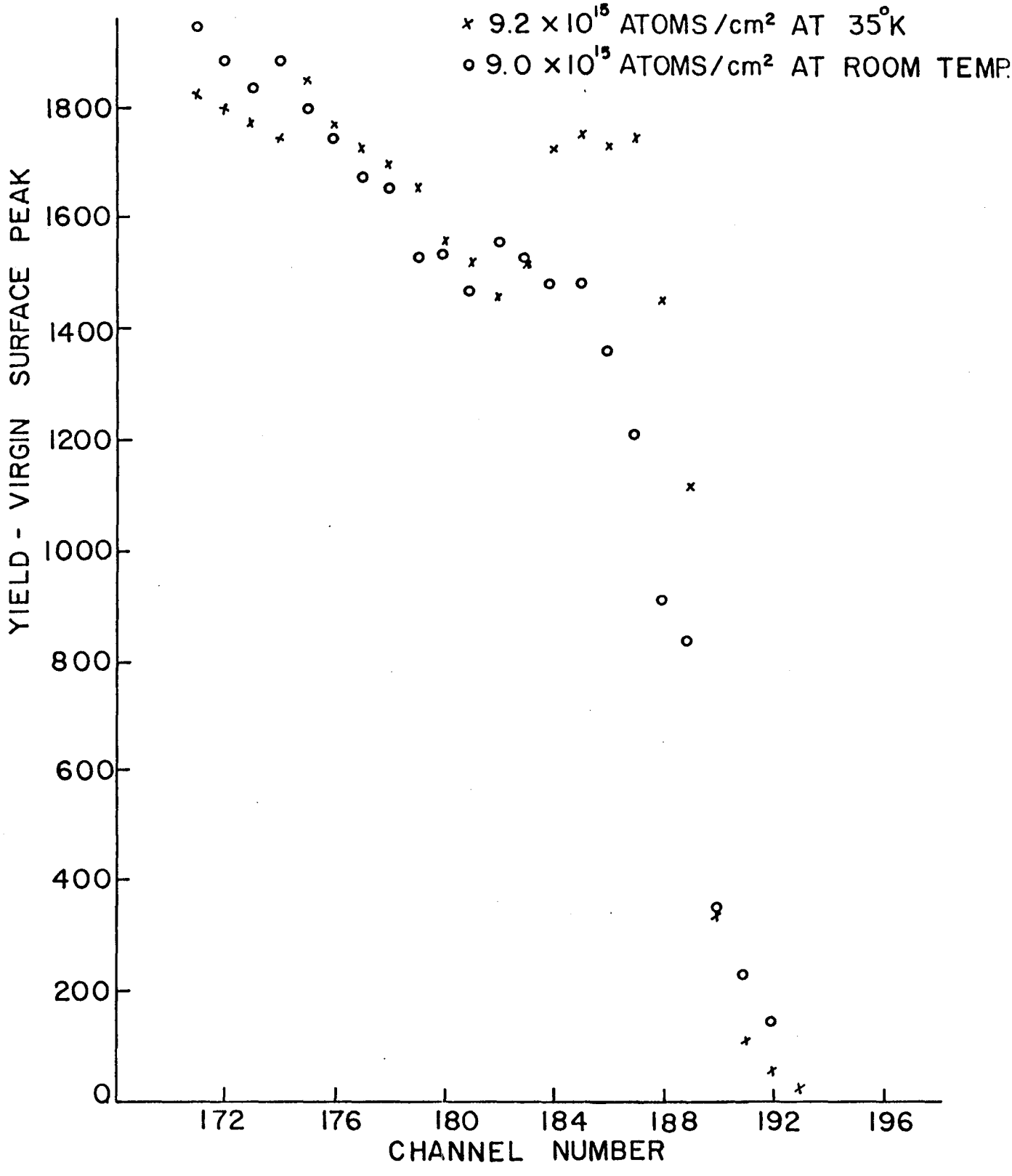

FIGURE 22. Same as Figure 20, but the surface peaks from the unimplanted spectra have been subtracted.

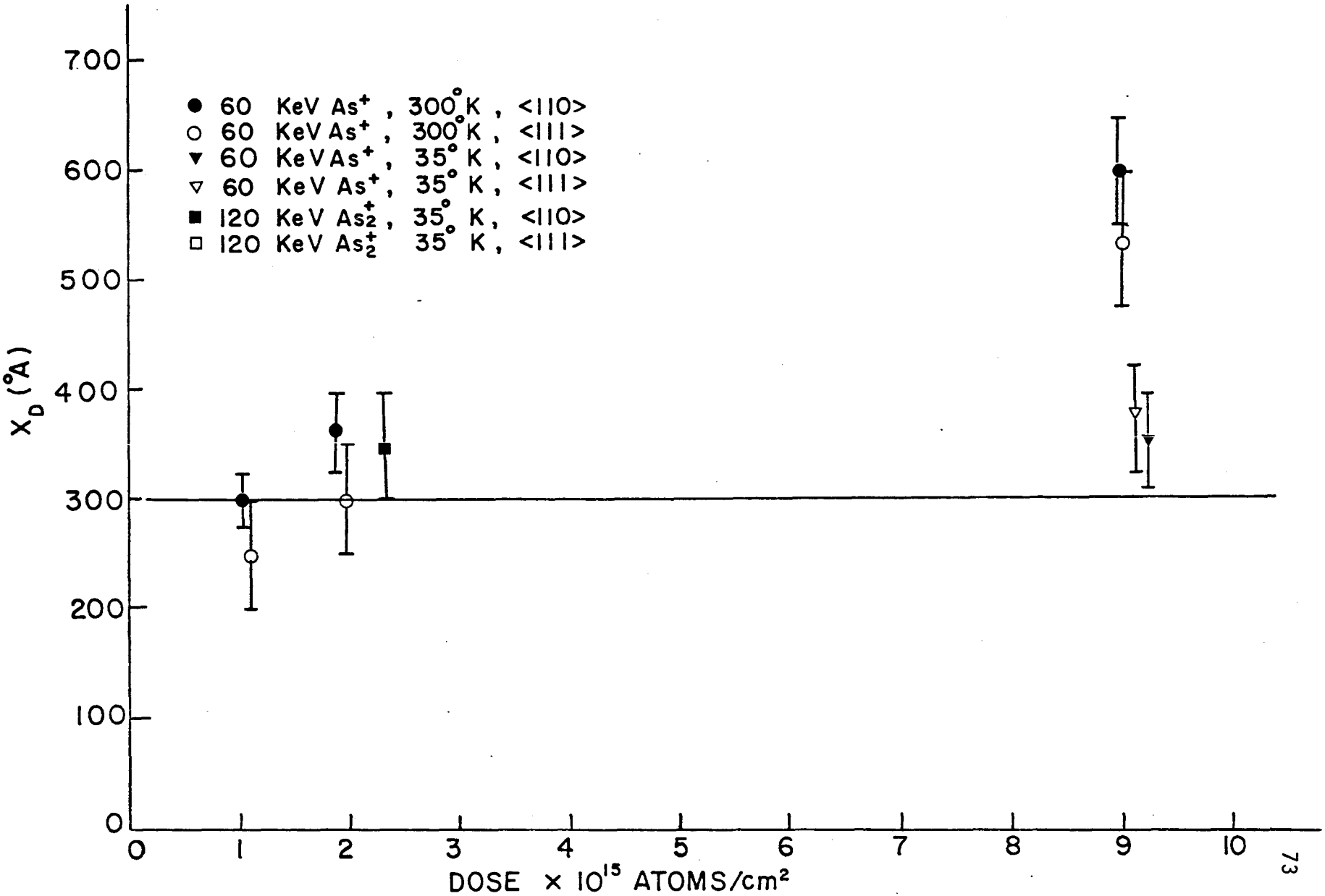

FIGURE 23. The depth of damage, X_D, vs. dose. The solid line corresponds to the depth within which most of the damage is contained, as calculated by a Monte Carlo technique.(44)

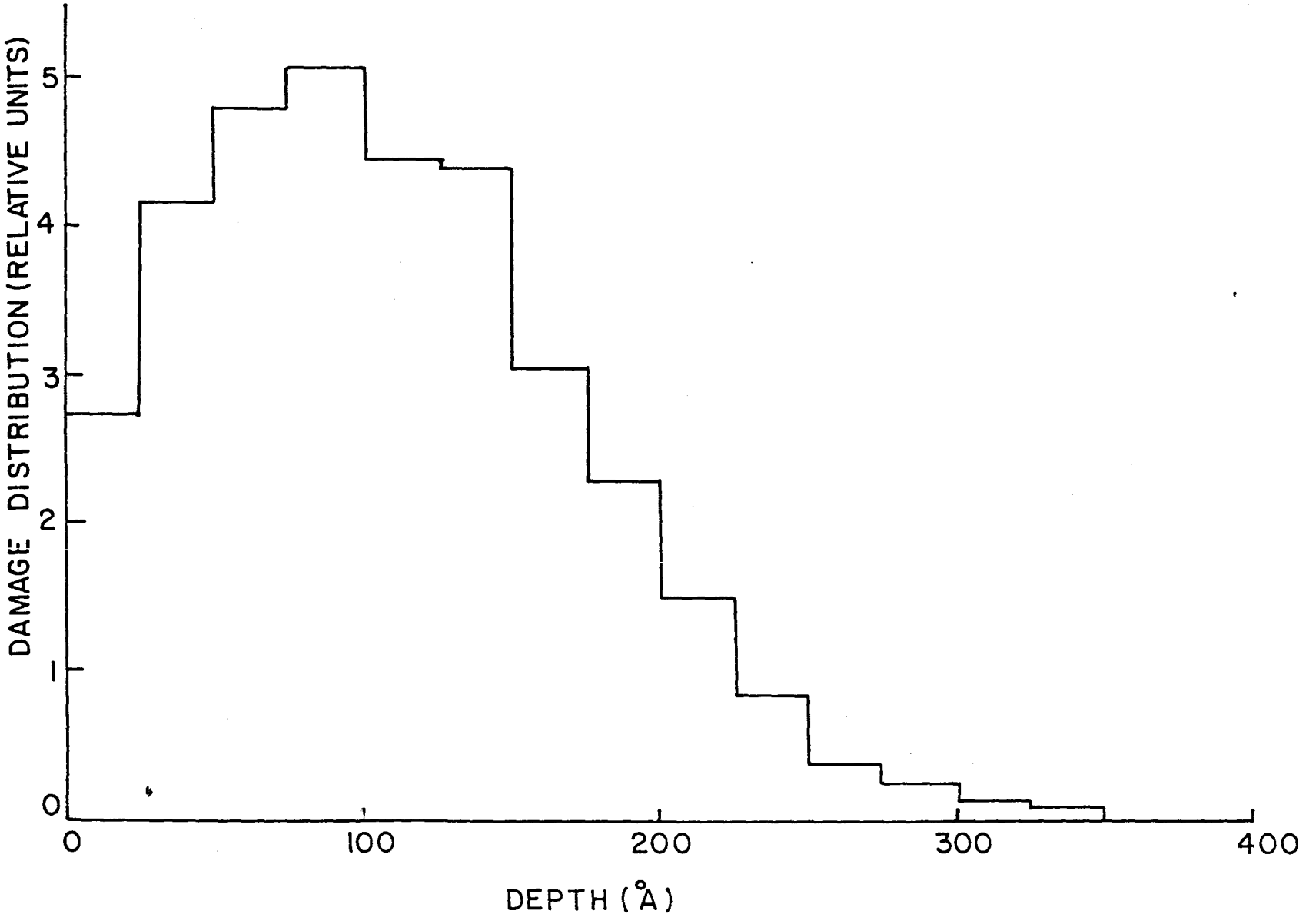

FIGURE 24. Damage distribution of 60 KEV As^+ in Fe, calculated using a Monte Carlo technique.[44]

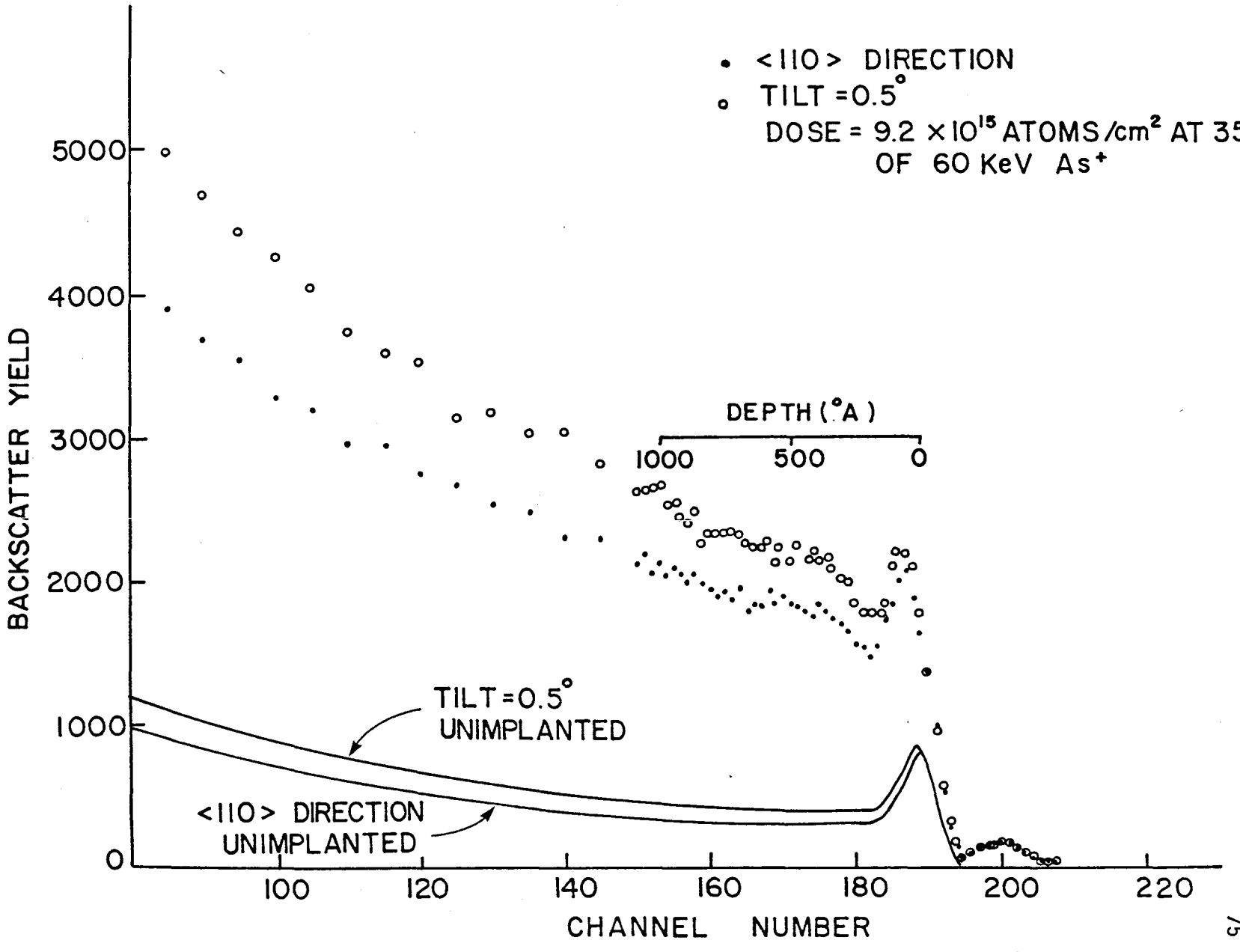

FIGURE 25. Backscatter yield showing the effects of tilting the 1.0 MEV He^+ beam .5° off axis.

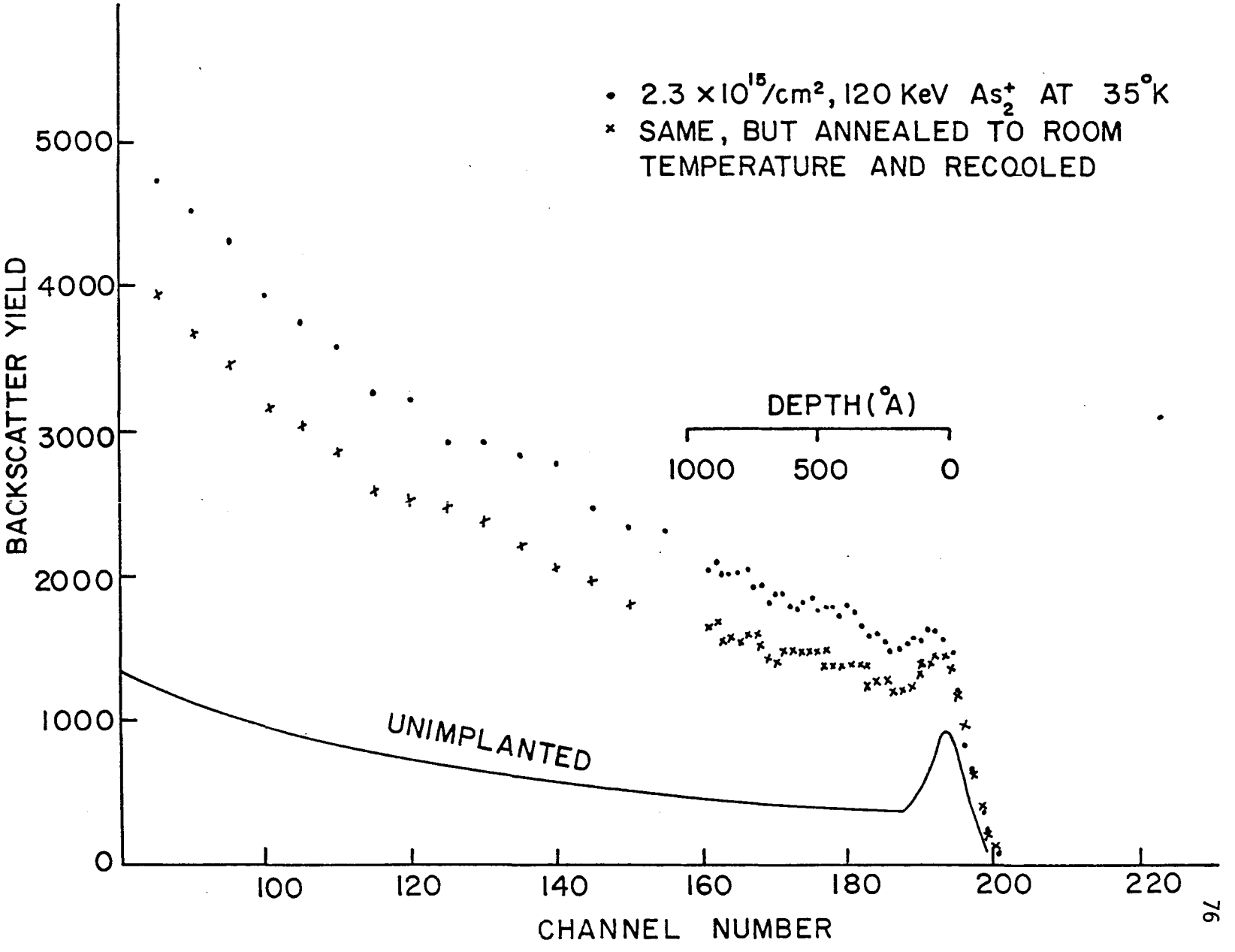

FIGURE 26. Spectra showing the effects of a 300°K anneal on a sample implanted and analyzed initially at 35°K.

REFERENCES

1. J.D. Lee, Rept. No. UCID-15944 (1971).
2. D.J. Rose, Rept. No. ORNL-TM-2204 (1968).
3. See for example, J.W. Menter, D.W. Pashley, A.E.B. Presland, "Properties of Reactor Materials and the Effects of Radiation Damage", William Clowes and Sons Limited, London (1962).
4. D.W. Pashley, A.E.B. Presland, Phil. Mag., 6, 1003 (1961).
5. J.W. Mayer, L. Eriksson and J.A. Davies, "Ion Implantation in Semiconductors", Academic Press, New York (1970).
6. F. Eisen in "Channeling in Solids", edited by D.V. Morgan (John Wiley and Sons, England, 1973), Chapter 14.
7. M. Gettings, O. Meyer and G. Linker, Rad. Eff., 21, 51 (1974).
8. P.P. Pronko, Nucl. Inst. and Meth., 132, 249 (1976).
9. C. Cawthorn and E.J. Fulton, Nature, 21b, 575 (1967).
10. D.G. Martin, Proc. Brit. Nucl. Energy Soc. Conf. on Nucl. Fusion Reactors, Abingdon, England (1970).
11. A. Omar, McMaster University, private communication, 1977.
12. M.T. Robinson and O.S. Oen, Conf. Proc.: Le Bombardement Ionique, ed. by J.J. Trillat, C.N.R.S., Paris (1962).
13. M.T. Robinson and O.S. Oen, Phys. Rev., 132, 1385 (1963).
14. G.R. Piercy, F. Brown, J.A. Davies, and M. McCargo, Phys. Rev. Letts., 10, 399 (1963).
15. H.O. Lutz and R. Sizmann, Phys. Letts., 5, 113 (1963).

16. J. Lindhard, Matt. Fys. Medd. Kgl. Danske Videnskab Selskab, 14, 34 (1965).

17. J.H. Barrett, Phys. Rev. B, 3, 1527 (1971).

18. E. Bøgh, Can. J. Phys., 46, 653 (1968).

19. L.C. Feldman and D.E. Murnick, Phys. Rev. B, 5, 1 (1972).

20. Y. Quéré, Rad. Eff., 28, 253 (1976).

21. B.C. Masters, Central Electricity Generating Board, Berkeley Nuclear Laboratories (1964).

22. C.A. English, B.L. Eyre and M.L. Jenkins, Nature, 263, 400 (1976).

23. E.A. Little, Int. Metal Rev., 204, 25 (1976).

24. K.B. Winterbon, P. Sigmund, and J.B. Saunders, Matt. Fys. Madd. Vid. Selsk., 37, 14 (1970).

25. P. Sigmund, Appl. Phys. Lett., 25, 169 (1974).

26. K.B. Winterbon, "Ion Implantation: Range and Energy Distributions", Vol. II, (Plenum Press, 1975).

27. P. Sigmund, Rad. Effects, 1, 15 (1969).

28. P.G. Lucasson and R.M. Walker, Phys. Rev., 127, 485 (1962).

29. See for example, D.A. Thompson and R.S. Walker, Rad. Eff., 30, 37 (1976).

30. P.P. Pronko, J. Bottiger, J.A. Davies and J.B. Mitchell, Rad. Eff., 21, 25 (1974).

31. J. Nihoul in "The Jülich Conference on Vacancies and Interstitials in Metals" (North Holland, 1970), pg. 839.

32. E.W. Muller in "The Jülich Conference on Vacancies and Interstitials in Metals" (North Holland, 1970), pg. 557.

33. J.A. Davies, L.M. Howe, D.A. Marsden and J.L. Whitton, Rad. Eff., 12, 247 (1972).

34. L.C. Feldman and J.W. Rogers, J. Appl. Phys., 41, 3776 (1970).

35. P.P. Pronko and K.L. Merkle, "Applications of Ion Beams to Metals", ed. by S.T. Picraux, E.P. Eernisse, and F.L. Vook (Plenum Press, N.Y., 1974).

36. E. Bøgh, Proc. Roy. Soc. (London), A311, 35 (1969).

37. J. Lindhard, M. Scharff and H.E. Schiott, Kgl. Danske Videnskab, Matt.-Fys. Medd., 14, 33 (1963).

38. M. Schmorak and E. Bøgh, "Hyperfine Structure and Nuclear Radiations", ed. by E. Matthias and D. Shirley (North-Holland, Amsterdam, 1968) pg. 712.

39. B. Deutch, "Hyperfine Interactions in Excited Nuclei", ed. by G. Goldring and R. Kalish (Gordon and Breach, N.Y., 1971).

40. F.H. Eisen and J. Bottiger, Appl. Phys. Lett., 24, 3 (1974).

41. See for a discussion, D.V. Morgan in "Channeling", ed. by D.V. Morgan (John Wiley and Sons, 1973).

42. J.F. Ziegler and W.K. Chu, "Atomic Data and Nuclear Data Tables", 13, 463 (1974).

43. F.H. Eisen, G.J. Clark, J. Bottiger and J.M. Poate, Rad. Eff., 13, 93 (1972).

44. N.G. El-Agizi, Master's Thesis, McMaster University (1975).

45. See for example, R.M. Walker, "Radiation Damage in Solids" (Academic Press, London, 1962).